# Novel Fission Track Detection for Identification and Characterization of Special Nuclear Materials

**A Dissertation Presented for the**
**Doctor of Philosophy**
**Degree**
**The University of Tennessee, Knoxville**

**Jonathan Allen Gill**
**December 2017**

Copyright © 2017 by Jonathan A. Gill
All rights reserved.

# DEDICATION

To my family, mentors, friends, Soldiers, and peers, you have made me who I am and made this work possible. Thank you. I hope that this initial contribution is the beginning of a lifelong contributing effort to the greater body of knowledge.

# ACKNOWLEDGEMENTS

Foremost, I would like to thank my advisor and committee chair, Dr. Howard Hall, for his support throughout this process. The trust he placed in me when accepting me as a Master's student on my second day of graduate school at the University of Tennessee and subsequent selection for work with BWX Technologies made all of this work possible and allowed me to start in earnest, my life long goal of becoming a scientist.

I would also like to thank my other UT committee members Dr. Thomas Meek, Dr. Joe Stainback IV, and Dr. John Auxier II for being on my committee and giving me honest feedback and helping guide me through this project. Their time and recommendations were crucial to the completion of this work.

Special thanks to Dr. Keith Rider. If I had to place a number on it, I would say we averaged an hour a day for 18 months straight discussing ideas, reviewing data, and vetting results. Many times I would kick myself for not coming up with ideas you suggested, or be saved/pulled back from spiraling into something interesting but not relevant to the dissertation. Without your vital support, at best this project would have taken three times as long, and at worst the project would have failed on the time and budget available. Thank you for your mentorship and friendship.

To Dr. Kevin Hour, thank you for enabling this project. Without your support it could have never happened and without your motivation, enthusiasm, and counsel it would have been a much more difficult, if not impossible road.

As with accomplishments, it’s a team effort and I have many to thank. I learned long ago, I'm not great as a single person, but with a team of people, many great things can be achieved. Cody Campbell, thank you for your help and training with AutoCAD and Inventor. Virginia Gibson, thank you for your gamma spectroscopy, decay chain analysis, and analytical chemistry work. Cody J. Havrilak, thank you for optical microscope assistance. Ken Gordon and Samuel G. Love, thank you for helping me with experimental design and getting the real work done. To both of you, thank you for taking the dose that I didn't have to take. Peter Macasa thank you for also getting actual work done and being my hands, a good number of hours were spent finding ways to get it done. William A. McInteer, thank you for the lab space and help with a number of logistical issues with life working in lab space. Debra L. Porter, thank you for helping with all of the stuff that isn't the technical work. There's so much admin and paperwork that goes into everything and you made me feel welcome at the LTC. Dr. Steven Younghouse, thank you for being a sounding board for some of the crazier ideas and helping with making my narrow Skynet. Dr. Maik Lang, thank you for discussion about heavy ions and facilitating work outside UTK.

To my undergrads, Hadyn Daugherty and Loraine Ilia, you both did a lot in a short period of time. I wish we could have gotten more time to do more but apparently 10 hours of research a week is the appropriate amount of work for a fully loaded undergrad with 50 plus hours of academic work. All that silly foundational learning getting in the way of research.

To Dr. Matthew Cook, we probably complained to each other as much as we got work done, which is really saying something given the number and scale of computer models that were run. Thank you for being the computer guy and thanks for many hours on the phone.

Lastly, I traveled a lot between Virginia and Tennessee, to Emilie Fenske and Adam Stratz, crashing on your couches let me work all hours of the night in the microscope lab and I apologize for any/many times I woke you up at o'dark thirty.

If I missed you, blame me for failure and I apologize, your contribution is important... I just have the memory of a gold fish.

Lastly, I want to eternally thank the Soldiers I served with, my mentors, friends, and family for helping shape me into who I am today. Without them I wouldn’t be me.

*It doesn't matter how beautiful your theory is, it doesn't matter how smart you are. If it doesn't agree with experiment, it's wrong.* -Richard Feynman

# ABSTRACT

Fission track detection and analysis is used primarily in nuclear safeguards to identify special nuclear material. Identification of isotopic ratios is a crucial step in understanding the intended use of nuclear material and the nature of the materials production cycle. Unfortunately, this methodology uses etchable track detectors that require significant expertise and intensive labor to process.

This study developed a novel method using lithium fluoride (LiF) as a fluorescing nuclear track detector to conduct fission track analysis for isotopic prediction of uranium enrichment. Individual latent tracks produced by fission products were observed in LiF for the first time. These tracks were identified using fluorescence microscopy with a confocal laser scanning microscope. Specifically, lithium fluoride's $F_2$ and $F_3^+$ defects were excited and observed for fluorescing emission. These observations required the use of highly sensitive detectors that could maintain at least a one to ten signal to noise ratio while detecting single photon signal. Fission tracks were verified with concurrent $^{252}Cf$ alpha tracks and agreement with variations in exposure times.

Experiments with uranium fuel glued to LiF detectors were used to predict enrichment. These samples were exposed to $10^{14}$ neutrons in a custom irradiator and then particles were characterized based on the number of tracks observed by the confocal laser scanning microscope. Predictions of uranium isotopes required calculation of particle mass contributing significantly to error. Seven of ten particles fell with error of prediction, two of which were depleted uranium samples and had predicted track counts of less than one per fuel grain.

This work proves the viability for a new method of identifying particles with fission track analysis. It reduces the work hours required to analyze an environmental sample for fissionable material by removing the need to etch traditional solid state nuclear track detectors.

# TABLE OF CONTENTS

CHAPTER I: INTRODUCTION ..... 1
CHAPTER II: BACKGROUND ..... 4
Solid State Nuclear Track Detectors ..... 4
Thermally Stimulated Luminescent Detectors ..... 13
Optically Stimulated Luminesce ..... 14
Lithium Fluoride ..... 16
Confocal Laser Scanning Microscope ..... 22
Excitation, Emission, and Resolution ..... 23
Inverted Sample Setup ..... 29
Sampling Parameters ..... 29
Nuclear Physics Modeling Codes ..... 32
MCNP ..... 32
SRIM ..... 32
CHAPTER III: ALPHA TRACKS ..... 34
Alpha Sources ..... 34
Experimental Method ..... 35
Results ..... 40
Analysis ..... 41
Conclusion ..... 43
CHAPTER IV: CALIFORNIUM FISSION TRACKS ..... 45
Experimental Method ..... 45
Results ..... 48
Analysis ..... 51
Conclusion ..... 60
CHAPTER V: URANIUM FISSION TRACKS ..... 61
Experimental Method ..... 61
Results ..... 68
Analysis ..... 72
CHAPTER VI: ENRICHMENT RELATIONSHIPS ..... 74
Future Work ..... 77
REFERENCES ..... 79
VITA ..... 85

# LIST OF TABLES

Table 1. List of measured critical angles for various etchable SSNTD for $^{252}$Cf SF fragments and $^{235}$U thermal neutron induced fission fragments. Efficiencies assume a $2\boldsymbol{\pi}$ geometry. ..... 12
Table 2. LiF physical property values used for calculations and design of experiments. ..... 19
Table 3. List of reported impurities in single LiF crystals used in this work. Crystals have a nominal mass of 167.2 mg. Values evaluated and reported by Precision Micro-Optics Inc. ..... 21
Table 4. A list of objectives and associated parameters available on this the TCS SP8 CLSM. Numerical aperture (NA) is a dimensionless number that describes the range of angles over which the objective can collect light. NA is therefore closely related to the working distance (WD) by NA = WD/objective diameter. All objectives are in-line with a built-in 10x lens on the microscope. Best resolutions are evaluated for 488 nm light. ..... 29
Table 5. A list of isotopic quantities and known alpha decay energies for alpha radiation contributors in the electroplated Cf source. ..... 36
Table 6. Naming and experiemental parameters for Cf exposures of LiF and $Al_2O_3$:C,Mg. ..... 47
Table 7. NIST $U_3O_8$ standards used in experiments and their respective isotopic atomic percent. ..... 65
Table 8. Model results for particles in the most intense flux position in the sample ports, as shown in the third position from the bottom of the sample port. Uranium enrichments selected comprise the majority of samples. Track counts use a $4\pi$ geometry. ..... 69
Table 9. Reported observations and calculations for fission tracks from particles identified at various enrichments. Calculations use a $2\pi$ minus particle surface area detector geometry and particle size using an ellipsoid estimation. ..... 72
Table 10. Reported observations and calculations for fission tracks from particles identified at various enrichments. Calculations use a $2\pi$ minus particle surface area detector geometry and particle size using an ellipsoid estimation. ..... 75

# LIST OF FIGURES

Figure 1. The sequential process of identifying and measuring isotopic information from suspected nuclear fuel particles using fission track detection. ..... 6
Figure 2. (a) and (b) are optical images. (c) and (d) are SEM images. (a) and (c) are images of the same particle's fission tracks. (b) and (d) are images of the same particle's fission tracks. Fission tracks were produced from uranium particles <1.5 μm in diameter that were irradiated with approx. 5 x $10^9$ thermal neutrons and 1 x $10^{10}$ fast neutrons. Detectable fission tracks were created by etching a plastic detector with 6 M NaOH, 4% $Na_2CO_3$ mixture at 60 ± 0.1 °C [9]. ..... 7
Figure 3. This fission track detection is under an optical microscope showing uranium oxide particles of 800 μm diameter containing 10% $^{235}U$. Numbers indicate the number of counted tracks for each particle [10]. ..... 8
Figure 4. Microscopic images of fission tracks from uranium particles on polycarbonate (Makrofol) etched with NaOH showing the effect of enrichment on the track star: natural (a), 10% enriched (b), and 85% enriched (c) [12]. ..... 8
Figure 5. Effects of etching times on a Semadeni industrial plastic detector etched with 6 M NaOH, 4% $Na_2CO_3$. Track stars are observed under optical inspection at 50x. Each image is a z-projection stack of the same volume projecting 15 images for a total depth of 2.25 μm [9]. ..... 10
Figure 6. Demonstrates various attack angles of incident ions relative to the effects of bulk and track etching rates. (a) shows an undetectable track with an angle of attack less than the critical angle, (b) shows a track at the minimum detection limit with an angle of attack equal to the critical angle, (c) shows a detectable track with an angle of attack greater than the critical angle, and (d) shows an easily detectable track with an angle of attack normal to the detector surface [5]. ..... 11
Figure 7. (a) is a typical configuration of a single sided polycarbonate SSNTD and (b) is a typical configuration of a two sided polycarbonate SSNTD. ..... 13
Figure 8. The glow curve for LiF:Mg,Ti. Numbered peaks represent different trap depths and different defect types. For most TLDs, multiple glow peaks are present and dopants can shifted peaks and also may improve peak resolution [22]. ..... 14
Figure 9. Absorption spectra for LiF irradiated with 275 kGy $\gamma$-ray, 750 kGy 31 MeV Ne ions (5x$10^{11}$ $cm^{-2}$), and 150 Gy 1400 MeV U ions ($10^{10}$ $cm^{-2}$). The band positions of different color centers and colloids are indicated. The $F_3$ and $F_4$ bands are clearly separated from the $F_2$ band for $\gamma$ exposure, however ion beams induce broadening from 350–500 nm region [37]. ..... 17
Figure 10. Compares excitation and emission dependences on temperature for LiF irradiated with 3 MeV electrons. Inspections occurred at 77 K. Absorption or emission coefficients are solid lines and best-fit (Gaussian) curves are

dashed lines. For (a) and (b) irradiation occurred at room temperature (RT) with $4.5x10^4$ Gy. (b) the photoluminescence spectra was excited at 457.9 nm. For (c) and (d) irradiation occurred at 213 K with $1.6x10^5$ Gy. (d) the photoluminescence spectra was excited at 457.9 nm. $F_3^+$ to $F_2$ creation is inversely dependent on temperature [38]. .....18
Figure 11. Various defect structures found in LiF [39].....18
Figure 12. External Transmittance curve for Lithium Fluoride Crystals as per the material vendor [40]. .....20
Figure 13. Diagram of the light path of a confocal microscope. Light travels bi-directionally though the objective with adjustable focal planes allowing the microscope to bring various layers within the working distance of the objective into focus. The pinhole aperture in front of the detector, the focal distance, and the wavelength of fluorescing light define a raw collection voxel's dimensions [43].....23
Figure 14. Diagram of an annotated upright Lecia TCS SP8 CLSM. The system used for this work is inverted variant of the diagramed microscope. Components listed in the diagram are the following: (1) White light laser (WLL), (2) Acousto-optical tunable filter, (3) Infrared Laser*, (4) Electro-optical modulation*, (5) Ultraviolet laser (UV), (6) Direct Modulation*, (7) STED laser*, (8) Acousto-optical beam splitter*, (9) FRAP Booster, (10) IR laser incoupling*, (11) UV laser incoupling CS2 UV optics, (12) STED laser incoupling*, (13) FOV Scanner with Tandem Scanner, (14) Scan optics with alternative UVIS, HIVIS, VISIR coating, (15) Scan field rotation (Abbe-König rotator), (16) Reflected light detection PMT in non-descanned position*, (17) Objective lens, (18) Transmitted light detection PMT in non-descanned position, (19) Square confocal pinhole, (20) Fluorifer disc, (21) Outcoupling with X1 port, (22) External detection*, (23) Prism-based dispersion, (24) SP detector with spectrophotometer arrangement, and (25) Two photo-multipliers (PMTs) and three hybrid photo detectors (HyD) [44]. .....24
Figure 15. Picture of Lecia TCS SP8 CLSM used for this work at the University of Tennessee Advanced Microscopy and Imaging Center.....25
Figure 16. A basic schematic of the HyD [45]. Due to the vacuum region and the semiconducting electron gain region the photon efficiency is very close to the quantum efficiency of the cathode. Additionally, the straight line relationship between the cathode and the semiconductor means that the pulse width is minimized and time gating can reasonable achieve nanosecond resolution.....27
Figure 17. The PSF is illustrated by two different objective diameters. In (a), the large objective diameter results in a large angle of light from the focal point which is defined as a high NA. In (b), the objective diameter is small resulting in a smaller angle of light from the focal point, therefore a lower NA. Also, the airy disc is more recognizable in (b) since a lower NA means a large airy [46].....28

Figure 18. A diagram of the light path through a typical sample. The green and red lines are excitation and emission light directions, respectively. The objective lens is immersed in oil. Layers with dimensions are to scale. The region of interest is typically surface B however, when using longer working distances surface A can be investigated. ..... 30
Figure 19. A vertically exploded drawing of the right cylindrical collimator for Cf exposures. The FNTD is orange and placed on top of the spacer. The Cf source is red and placed in-between the source mount and vacuum flange. Ions traveled along the 7/16" diameter cylindrical column to impinge on the detector. Dimensions for the spacer shown are for the longer of the two configurations. Drawing is not to scale. ..... 37
Figure 20. Annotated pictures of the vacuum chamber and collimator prepared for assembly. (a) shows the assembled collimator ready to be raised and clamped into place. (b) close-up picture of the collimator ready to be raised and clamped into place. (c) dissembled collimator showing both spacers and the vacuum flange with Cf source mount. The Cf source and LiF disc are in their respective positions in all pictures expect for the short spacer in (c). .. 38
Figure 21. Sample preparation for confocal inspection. Similar to Figure 18 excitation and collection occurs through the same objective lens with a glass coverslip holding the sample above the objective. Immersion oil is used as the coupling liquid between all solid mediums. ..... 39
Figure 22. $F_2$ fluorescence from alpha damage in LiF from Cf. The surface of the crystal is on the left side of the images along the x-axis and the alpha tracks are traveling from the surface into the crystal along the positive z-axis. (a) shows non-thermally pretreated LiF with a poor SNR. (b) shows thermally pretreated LiF with a significantly improved SNR from 4-M-60-L. In thermally pretreated LiF, alphas are counted and found to agree with expected ratios with fission tracks. Comparatively, the surface brightness in (a) is 28 times more intense than in (b), while the alpha brightness does not change appreciably. ..... 41
Figure 23. Raw latent alpha track intensity distribution from Cf decay alpha tracks and intensities after background subtraction. Intensity is the total summed intensity of the ROI placed around the track. ..... 42
Figure 24. A plot of the LiF samples listed in Table 6 comparing anticipated areal density to observed areal density. Anticipated values fall on the bold diagonal line. Standard error and a vacuum pumping uncertainty are applied to observed densities. The lowest fluence has an observed density of 4.17 x $10^4$ track $cm^{-2}$. The 3 x $10^7$ track $cm^{-2}$ anticipated areal track density data point was exposed with the smaller spacer; its error includes a larger exposure time uncertainty. ..... 49
Figure 25. images of LiF, sample 4-M-1020-L, taken 3.6 ± 0.5 μm into the surface of the detector. (a) is collection of $F_2$ signal. (b) is collection of $F_3^+$ signal. (c) is collection of $F_4$-like signal. Each spot is a fission track. Alpha tracks are

not easily observable in (a) due to contrast and brightness settings. Scale bars denote 5 μm. ..... 51
Figure 26. images of $Al_2O_3$:C,Mg taken 3.6 ± 0.5 μm into the surface of the detector. Each spot is either an alpha track or fission track. Due to high signal from alpha tracks and relatively low signal difference between alphas and fission tracks, a lower intensity exposure is shown in (b). (a) is collected from 4-M-1020-A. (b) is collected 4-M-235-A, approximately a 77% reduction in track density form (a). Scale bars denote 5 μm. ..... 51
Figure 27. Images are cross-sectional 30.8 μm x 10.5 μm x 16.1 μm projections from LiF sample 2-M-20-L. Images are the raw intensity data utilizing the maximum intensity voxel in projection to compress the y-axis into a single frame. (a) is a monochromatic image of $F_3^+$ emissions. (b) is a monochromatic image of $F_2$ emission. The irradiated surface is the bright edge along the bottom of the images. The incident ions are in the positive z direction. An alpha track is present on the left side of (b) but is not visible in (a). ..... 52
Figure 28. Latent fission track intensity distribution from Cf SF from thermally pretreated samples. Intensity is the total summed intensity of the ROI placed around the track in each image. Intensities are raw intensity values observed within the ROIs. ..... 53
Figure 29. Fluorescence intensity versus depth plots for six randomly selected tracks. The surface of the detector starts at depth zero. The graphs highlight the inconsistent decrease in intensity of single tracks. ..... 56
Figure 29. SRIM modeling of LET for the pair of most abundant, the lightest, and the heaviest $^{252}$Cf fission products as a function of penetration depth in LiF [56]. The thick dashed horizontal line is the threshold above which F-defect creations likely by columbic explosive dislocation, whereas decay of self-trapped excitons is more likely below this threshold [34]. The dark vertical line represents the approximate depth at which the many ions are expected to produce significantly fewer fluorescing defects. This chart shows that while most tracks will have a roughly linear decreasing energy transfer to the crystal until the end of the track, at a point below 4.3 μm all tracks should have a nonlinear change in fluorescing intensity. Also, from models and indicated in this graph, no fission product is expected to penetrate deeper than 20.5 μm into the crystal and a significant majority will penetrate less than 16 μm. ..... 57
Figure 30. Average fission track fluorescence of 49 tracks from 4-M-235-L-A. Crystal surface is at zero depth. Tracks observed are an average of all tracks within a 40 x 40 μm area. In general, the area was randomly selected from the center of the irradiated surface. Exponential trend lines are fitted to each data set showing a similar behavior across the defect types with $F_4$-like behaving almost linearly. Each fits' coefficient of determination, $R^2$, is above 97% reflecting a good fit. Data is raw intensity collected. No background correction or other subtracts were performed. ..... 58

Figure 32. $F_2$ emission from a latent fission track. (a) is raw fluorescence data showing incoherent signal around the edges of the inner and outer regions of the track. (b) is the same track using a median filter to reduce noise thereby presenting a smoother and, due to the low light environment, overall reduced intensity. Per voxel, white is 0-1 intensity, light red is 2-7 intensity, and dark red is 8-32 intensity. ..... 59
Figure 35. Irradiator core drawing. The source port is the large center port. The sample ports are the four smaller ports arrayed around the center. Thin steel wire was wrapped and taped to the core for remote handling. Three threaded handling sockets allowed for removal from the irradiator incase the primary means of removal was not functioning properly. ..... 62
Figure 36. A diagram of the 110-gallon steel drum irradiator. The drum was filled with water to moderate the neutron field. ..... 62
Figure 37. MCNP model geometry (a) and thermal neutron flux (b) for the irradiator. A thermalization of roughly 12% was achieved in the sample ports from a $^{252}Cf$ sources. (b) shows only the core model with the neutron field slightly heterogeneous about the source. The source was modeled as a line source to best approximate the platinum wires containing the $^{252}Cf$. The flux fraction heat scale in (b) reads from top to bottom $2.9 \times 10^{-3}$, $3.8 \times 10^{-5}$, $6.8 \times 10^{-7}$, $1 \times 10^{-8}$, and $1.7 \times 10^{-10}$. ..... 64
Figure 38. SEM image of U200 on carbon tape to verify size of particles. Most particles are clearly a collection of smaller, submicron particles. ..... 66
Figure 39. Detector and fuel diagram shows a detector ‘sandwich’ around the fuel particles. Particles are adhered to the crystals with cellulose nitrate to maintain registration of particles. ..... 66
Figure 41. Images of the same xy-position with different z positions. (a) is an imagine of green fluorescent beads placed on the bottom of a blank LiF disc at stage position +177 µm. (b) is an imagine of green fluorescent beads placed on top of a blank LiF disc at stage position -492 µm. ..... 68
Figure 42. Images of 93.2% $^{235}U$ particles of 1.7 and 2.3 µm diameters with fission tracks observed in the LiF detector, originating from the fuel particles. Fuel was irradiated with $4 \times 10^8$ n $cm^{-2}$. Each image used individualized projection to best present particle and track signal. (a) is a reflected 488 nm light image projecting the max intensity voxel for a depth of 1.2 µm above and including the surface of the detector. (b) is $F_3^+$ signal summing the intensity for the first 9 µm of detector from the surface. (c) is $F_2$ signal projecting the max intensity voxel within the first 9 µm of detector from the surface. Scale bars are 5 µm. ..... 70
Figure 43. 0.48% $^{235}U$ enriched particle projecting a shadow approximate to its surface area, 56 µm by 35 µm. (a) shows $F_3^+$ signal in cross-section with tracks along the end of the particle protruding into the LiF surface. (b) shows the $F_2$ signal at a 45° viewing angle to show that the shadow of the particle blocks signal over 20 µm into the detector. ..... 70

Figure 44. images of 93.2% $^{235}U$ particles of 10 µm and 3 µm diameters with fission tracks observed in the LiF detector, tracks do not originate from the fuel particles. Fuel was irradiated with 4 x $10^8$ n $cm^{-2}$. Each image used a max intensity projection. (a) is a reflected 488 nm light image projecting the max intensity voxel for a depth of 11 µm above and including the surface of the detector. (b) is $F_3^+$ signal of the first 9 µm of detector from the surface. (c) is $F_2$ signal of the first 9 µm of detector from the surface. Scale bars are 5 µm.....71

# NOMENCLATURE AND TERMINOLOGY

| | |
|---|---|
| $Al_2O_3$:C,Mg | doped sapphire, synthetic corundum |
| CLSM | confocal laser scanning microscopy |
| Dwell Time | period of time a microscope collects light from a specific volume |
| FNTD | fluorescent nuclear track detector |
| LET | linear energy transfer |
| LiF | lithium fluoride |
| NA | numerical aperture, defined by the point spread function |
| OBJ | optical objective lens that gathers light |
| OSL | optically stimulated luminescence |
| OSLD | optically stimulated luminescence detector |
| PSF | point spread function |
| Raster | A rectangular pattern of parallel scanning lines |
| Image Stack | set of thin ‘2D’ images that are stacked to form a 3D image |
| SIMS | sputtering ion mass spectrometry |
| SNM | special nuclear material |
| SSNTD | solid state nuclear track detectors |
| TLD | thermal luminescent dosimetry |
| TSL | thermally stimulated luminescence |
| VIS | visible light spectrum |
| Voxel | discrete volume, a ‘3D pixel’ |
| WD | working distance, axial focusing range of a lens |

# CHAPTER I: INTRODUCTION

Nuclear security became a reality on July 16, 1945 with the Trinity test. Three weeks later, nuclear weapons bookended the largest war in human history. With Pandora's Box opened, nuclear weapons became the keystone of a four decade long standoff that for the first time in recorded history threatened our entire species. Fortunately, that standoff ended with an economic and diplomatic solution instead of our tried and true violent one. Unfortunately, Pandora's Box remains forever open and in the decades following the Cold War, nuclear terrorism and regional disputes have spawned a new threat. A threat that is often insidious, diffuse, and lethal.

Solutions to this nuclear threat are nontrivial and critically important to keeping the world from an unprecedented level of death and suffering. One key to this threat is information surety, specifically surety about nuclear weapons. If one is used or found in the wild, knowing where it came from, how it got there, and who owns it/used it will crucially inform decision makers to prevent the first use or next use. This is the charge of nuclear forensics.

> The threat of a nuclear terrorist attack on American interests, both domestic and abroad, is one of the most serious threats to the national security of the United States. In the wake of an attack, attribution of responsibility would be of utmost importance. Because of the destructive power of a nuclear weapon, there could be little forensic evidence except the radioactive material in the weapon itself.
>
> - Nuclear Forensics and Attribution Act 2010, Section 2. (1)

Even after 22 years of international effort the term "nuclear forensics" varies from organization to organization. And in the context of its importance, an accepted definition is essential to establishing a common understanding.

> Nuclear forensics is the technical means by which nuclear materials, whether intercepted intact or retrieved from post-explosion debris, are characterized (as to composition, physical condition, age, provenance, history) and interpreted (as to provenance, industrial history, and implications for nuclear device design).

- Nuclear Forensics: Role, State of the Art, Program Needs, 2012

The technical effort of nuclear forensics has many factors which must be addressed to identify nuclear material(s) confidently and understand the material for provenance. The following is a list of some of the most important solutions that are required for this technical effort. 1) Elemental and isotopic evaluation of fissile materials focusing on uranium and plutonium enabled by separation techniques capable of micron and below particle size distinction. 2) Measurement of chronometric signatures including micro-morphology and decay product ingrowth. 3) Impurity measurement of both natural and process generated impurities. 4) Morphological parameters of radioactive and nonradioactive materials at and below the micron scale. 5) Measurement and evaluation of radionuclides. When these technical results are compared to a library of known mines, special nuclear material manufacturing and machining processes, storage environments, and operations and maintenance programs they are then suitable for fusion with intelligence and law enforcement information to develop a confident and coherent assessment of attribution.

Successively, counter nuclear forensic considerations add dramatic complexity to this already difficult problem. Counter forensic is defined as means through which the origin or history of pre- or post-detonation material is obscured or leads investigators to false conclusions. Because of the motivations and implications of counter forensic, these efforts are kept under the opus of national security and thus state level information is controlled. Ideally, the technical effort of nuclear forensics would be able to also characterize counter efforts, either by using signatures that were not altered by the materials designer or by process signatures that counter forensics efforts impart to the material, and most often a combination of both. However, in practice this is very difficult and in practicum counter forensics efforts typically result in low confidence or inclusive forensics conclusions.

The particular aspects of nuclear forensics to which this work applies is pre-detonation isotopic characterization of special nuclear material, specifically

$^{235}U$ enrichment assay. Because latent signatures from fissions induced by neutrons are used, only fissile isotopes are suitable for investigation. Although, discoveries during method development indicate applications beyond fissile isotopes, to include alpha decay and ion emission resulting from neutron activation, this work does not pursue those paths to a useful outcome. The application of this work is envisioned in two ways: to provide an additional in-laboratory method for enriched particle identification, and more interestingly, to provide an in-the-field capability for overt international agents or domestic covert agents to quickly assess environmental samples for illicit or for non-civilian use enriched nuclear materials. In the latter case, initial in-the-field considerations were made during method development to reduce “carry-in” logistical overhead. This constraint is particularly challenging and is discussed in Chapter VI.

In counter forensics this work’s application remains in pre-detonation isotopic characterization but is specifically suitable for isolating particles of different enrichments. A particular scenario with utility is described as grain mixing of natural or civilian use material and weapons grade material. Application to this scenario is limited technically by the ability to fission $^{235}U$ in a reasonable period of time. This means that particles greater than 500 nm in diameter or 100 femtograms are the minimum capability of the tool but at these minimums high levels of enrichment or numerous moderately enriched particles are necessary to provide the minimum macroscopic cross-section for achieving a reasonable fission rate. Logistically, this application also requires a higher standard of particle control. And this particle, while reported by the Japanese, has not been tested with this specific system.

# CHAPTER II: BACKGROUND

## Solid State Nuclear Track Detectors

Solid state nuclear track detectors (SSNTD) are well researched and a number of books are available discussing their application and behavior [1], [2], [3], [4]. This family of detectors is based on physical phenomena that occur when radiation interacts with a detector medium typically causing ionization which creates a detectable latent signal. Ionization can also be indirectly caused by neutron or photon secondary particles, or directly by a charged particle, e.g. swift heavy ion or electron. In the case of heavy ion induced ionization, generally cylindrical are generated in the solid detector. In etched detectors, the most common type, these 1-2 nm physical tracks are enhanced to hundreds of nanometers through chemical etching for optical or electron microscopy inspection [5]. Tracks may also be observed using fluorescing nuclear track detectors (FNTDs) and fluorescing microscopy to examine radiation tracks [1].

SSNTDs have a variety of uses including environmental monitoring, occupational dosimetry, safeguards monitoring, nuclear medicine, archeology, and geology [5], [6]. When used in safeguards, nuclear fuel is examined with SSNTDs by placing suspected fuel particulate between detectors which will store track information from natural alpha decay, neutron activation byproducts, or most often, fission products from neutron induced fission. In nuclear medicine, efforts to develop high precision single cell dosimetry offer an excellent parallel to the high precision needs in nuclear safeguards [7]. The Heidelberg Ion Therapy Center's current research using individual track detection techniques is useful in this regard and is cited throughout this work.[1]

This study of FNTD principle utilizes lithium fluoride (LiF) which was the first solid state nuclear track detector [8]. Tracks were etched similarly to modern

[1] Additional information about the Heidelberg Ion Therapy Center is found online at https://www.klinikum.uni-heidelberg.de/The-technology.112985.0.html?&L=1 , last verified access on 6 May 2017.

etchable detectors; however materials used in modern swift heavy ion detection vary widely: muscovite mica, polycarbonate, polyethylene terephthalate, various glasses, and other insulating materials [5], [9]. In Figure 1 lays out the sequential special nuclear material (SNM) characterization process commonly employing etchable track detectors. Fissile material is placed on the detector and controlled in a way known as registration so that particles can be compared to tracks after neutron exposure and subsequent separation. Registration often requires techniques for particle control involving glues or sufficiently neutron resistant resin [9]. The sample and detector materials are then exposed to a neutron field appropriate to generate a large number of fission events per particle. The sample and detector are then removed from the field and separated so that fission tracks may be enhanced through chemically etching for examination [10].

Figure 2 shows etched fission track 'stars' from two different particles under optical and scanning electron microscopy (SEM). Automated methods are underdevelopment but current International Atomic Energy Agency (IAEA) protocol requires a technician to assess which particles are candidates for further analysis [9], [11]. Depending on the neutron fluence, fissile elements expected, expected isotopic quality of the particles, and particle sizes a technician may initially estimate the enrichment of the particle [10]. Figure 3 shows a field of stars in a detector from which a technician would select particles of interest and Figure 4 shows the effect of enrichment on the appearance of the etched tracks 'stars'. From these images and other published work, technicians can assess rough enrichment. Precise quantitative assessment of enrichment and analysis of other trace isotopes requires further analysis. A variety of methods are available to quantify isotopic and trace elemental.[2]

[2] These methods are most often various mass spectrometry techniques. As these are methods are covered extensively in many nuclear forensic texts, they are not explained in detail here. The most common of these are sputter ion mass spectrometer (SIMS), thermal ionization mass spectrometer (TIMS), inductively coupled mass spectrometer (ICP-MS), and more recently laser ablation inductively coupled mass spectrometer (LA-ICP-MS) [5].

The etching process is well researched for a number of track detectors, solvents, etching times, and temperatures [4]. The length, diameter, and angle of attack for each track is required for individual track analysis and when combined with etching rates a detector's critical track diameter, critical attack angle, and overall track detector efficiency may be calculated. The qualitative impact of etching rates can be seen in Figure 5 with increased etch time enhancing track appearance at 4 mins and beginning saturation of areas with high areal track density at 7 mins. This etching relationship is similar for all track detectors using standard chemical etching.

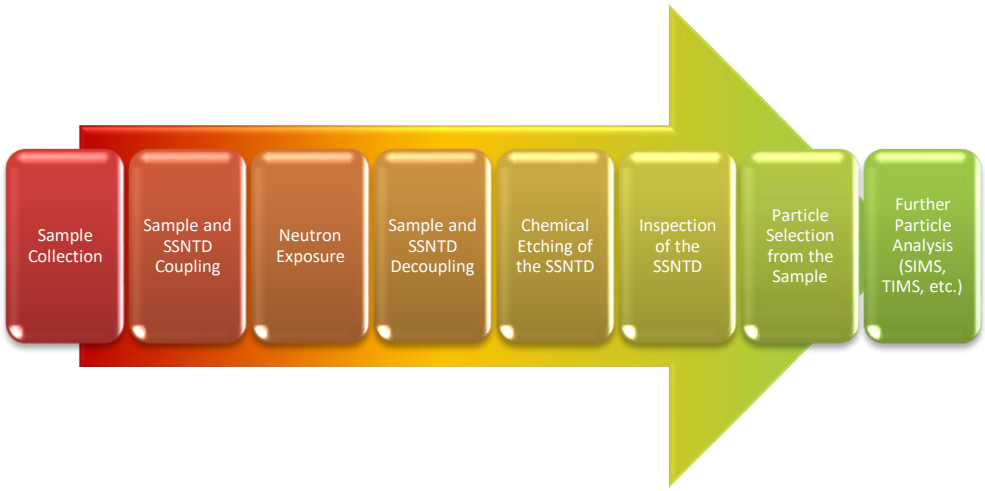



**Figure 1. The sequential process of identifying and measuring isotopic information from suspected nuclear fuel particles using fission track detection.**

An etchable detector's efficiency is the number of tracks observed in the detector divided by the number of heavy ions produced by a particle. Some relevant detector characteristics are not represented in this relationship like the neutron damage sensitivity, temperature stability, chemical stability, and temporal stability. However, this ratio is still a valuable tool for comparing etchable track detectors.

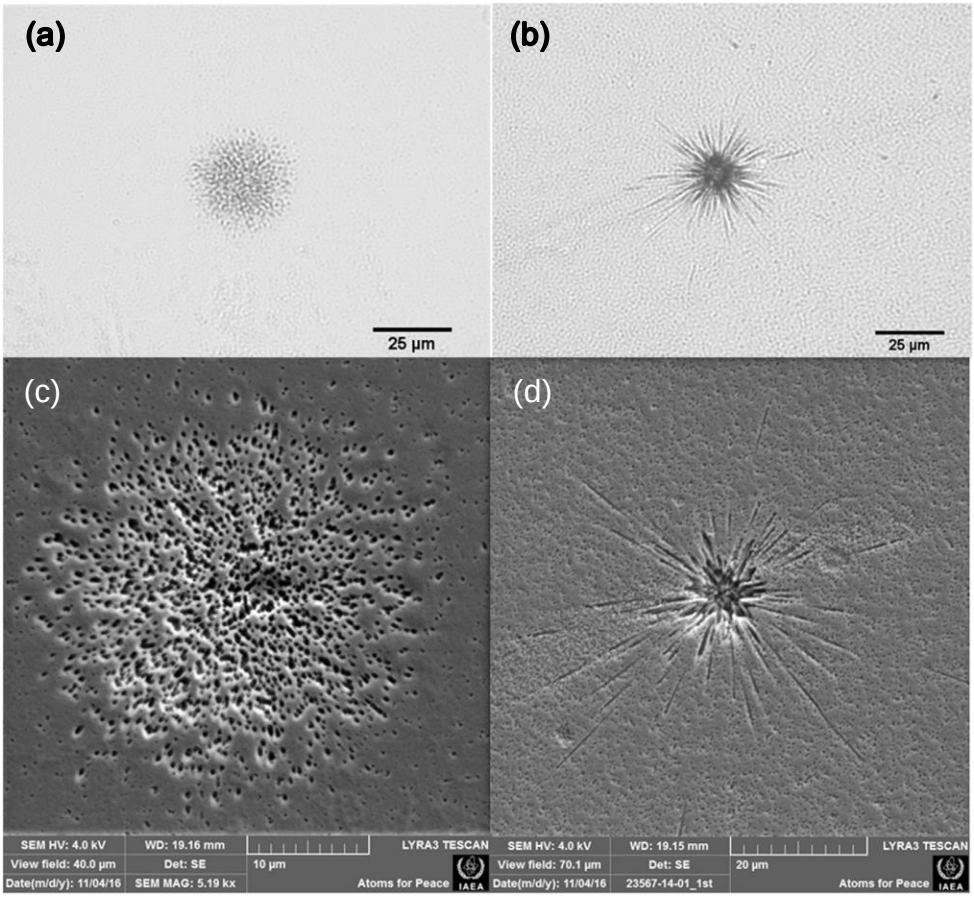



**Figure 2. (a) and (b) are optical images. (c) and (d) are SEM images. (a) and (c) are images of the same particle's fission tracks. (b) and (d) are images of the same particle's fission tracks. Fission tracks were produced from uranium particles <1.5 µm in diameter that were irradiated with approx. 5 x $10^9$ thermal neutrons and 1 x $10^{10}$ fast neutrons. Detectable fission tracks were created by etching a plastic detector with 6 M NaOH, 4% $Na_2CO_3$ mixture at 60 ± 0.1 °C [9].**

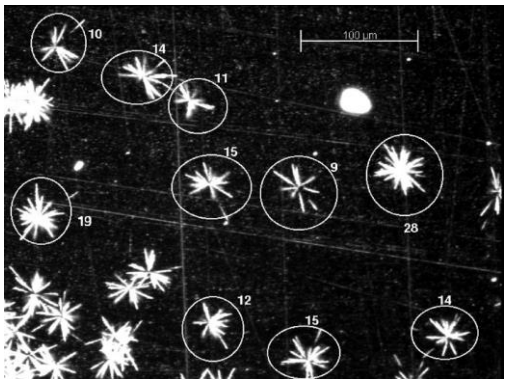



**Figure 3. This fission track detection is under an optical microscope showing uranium oxide particles of 800 µm diameter containing 10% $^{235}$U. Numbers indicate the number of counted tracks for each particle [10].**

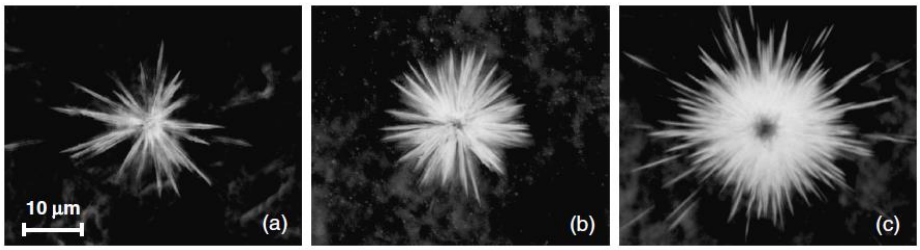



**Figure 4. Microscopic images of fission tracks from uranium particles on polycarbonate (Makrofol) etched with NaOH showing the effect of enrichment on the track star: natural (a), 10% enriched (b), and 85% enriched (c) [12].**

The actual number of heavy ions produced is described by the fission rate equation,

$$\boldsymbol{R = \sum_{i=j}^{n} \int \sigma_{fi}\ dE \int \Phi\ dE\ N_i} \qquad 1$$

where R is the total fission rate of the particle of fuel [fissions sec$^{-1}$], $\sigma_{fi}\ dE$ is the microscopic energy dependent fission cross-section for isotope i [cm$^2$], $\Phi\ dE$ is the neutron flux energy profile [cm$^{-2}$ sec$^{-1}$], $N_i$ is the atomic density of isotope i in the particle [cm$^{-3}$], and j, …, n are the various fissile isotopes in the particle. This rate is the real number of heavy ions produced by the fissile material.

The actual number of heavy ions to arrive at the detector, and are also detectable, is dependent on limiting factors that reduce the efficiency of the detector. These factors are the solid angle of the detector relative to the fuel particle (usually assumed $2\pi$), particle self-shielding (usually managed through restricted linear energy transfer), losses from materials between the fissile material and the detector (e.g. glues or plastics used to maintain geometry for registration), critical track angle, and minimum linear energy transfer (LET) to produce an etchable track in the ion. The minimum LET is mitigated in the case of fission ion as they are relatively energetic with total kinetic energies (TKE) >50 MeV and particles of interest will produce fission produces homogenously; therefore, a normal distribution of ions is expected from the surface of a particle. The remaining factors are readily described,

$$\boldsymbol{\varepsilon} = \begin{cases} \widehat{\boldsymbol{\Omega}}\,(\mathbf{1} - \mathbf{sin\theta_c}) & \mathbf{0 \le t \le t_c} \\ \widehat{\boldsymbol{\Omega}}\left(\mathbf{1} - \mathbf{sin\theta_c} - \frac{\mathbf{(t - R sin\theta_c)^2}}{\mathbf{2Rt}}\right) & \mathbf{t_c \le t \le R} \\ \widehat{\boldsymbol{\Omega}}\left(\frac{\mathbf{R}}{\mathbf{2t}}\mathbf{cos^2\theta_c}\right) & \mathbf{t_c \ge R} \end{cases} \quad (2)$$

where the detector efficiency $\varepsilon$ [%] is dependent on the critical angle $\theta_c$, R is the average ion range in the fuel particle [mg/cm$^2$], t is the thickness of the fuel particle [mg/cm$^2$], $t_c$ is the critical thickness $t_c = Rsin\theta_c$ of the particle [mg/cm$^2$], and restricted by the solid angle $\hat{\Omega}$ as a sector percentage [%] [13]. The critical angle for an etchable detector is the attack angle of an ion such that the etching of the surface $V_B$ and the etching of the track $V_T$ meet precisely at the point that removes all detectable track information, illustrated in Figure 6.

$$\boldsymbol{\theta_c} = \mathbf{arcsin}\left(\frac{V_B}{V_T}\right) \quad (3)$$

This relationship depends on the two etching rates to be constant. While this assumption is useful, it is understood that tracking etching rates vary by depth and that rate is dependent on the etchants surface reaction rate which is partly dependent on the amorphous character of that surface [14].

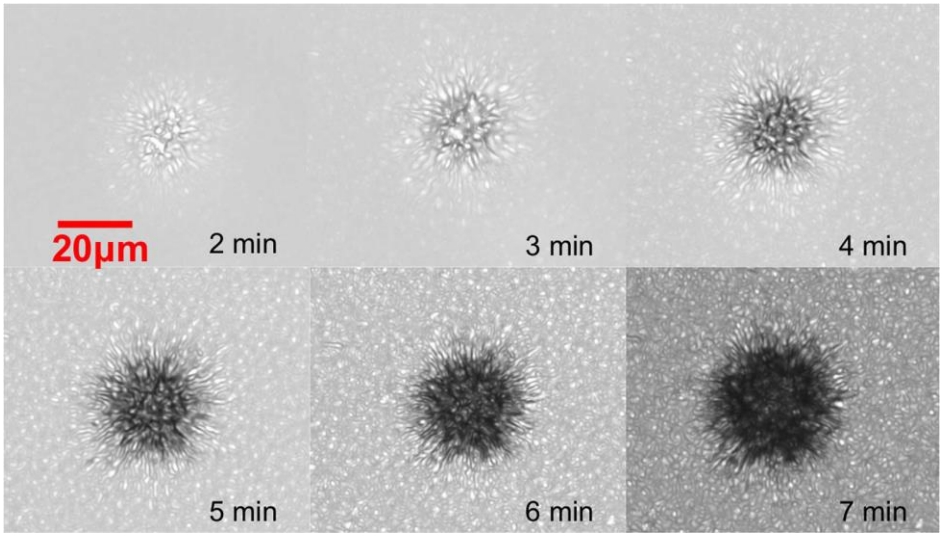



**Figure 5. Effects of etching times on a Semadeni industrial plastic detector etched with 6 M NaOH, 4% $Na_2CO_3$. Track stars are observed under optical inspection at 50x. Each image is a z-projection stack of the same volume projecting 15 images for a total depth of 2.25 µm [9].**

Fortunately, a large body of work has developed for etching parameters that can be used for comparison to values. Table 1 contains typical parameters for various SSNTDs. For this work, empirical measurements for critical angles are reported for both $^{252}Cf$ spontaneous fission (SF) fragments and $^{235}U$ thermal neutron induced fission fragments. In general plastic detectors have the best critical angles with the highest efficiency and are accordingly common in nuclear safeguards today [15].

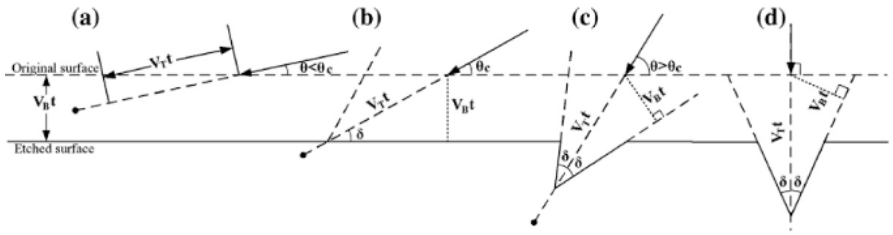



**Figure 6. Demonstrates various attack angles of incident ions relative to the effects of bulk and track etching rates. (a) shows an undetectable track with an angle of attack less than the critical angle, (b) shows a track at the minimum detection limit with an angle of attack equal to the critical angle, (c) shows a detectable track with an angle of attack greater than the critical angle, and (d) shows an easily detectable track with an angle of attack normal to the detector surface [5].**

Additionally, an improved control method uses electrochemical etching method to increase the track etching rate relative to the bulk etching rate by using two electrodes to effectively increase the etchants reaction rate inside the tracks [16]. This method increases the size of etched tracks roughly an order of magnitude, up to hundreds of microns, making optical detection of a fission track star easier. However, the loss in track fidelity precludes this method for direct comparison to this work.

Etchable track detectors registration is a crucial step in track detection where a thin film usually holds fuel particles in a stable geometry and the detector. During irradiation, the thin film with fuel and the detector are coupled, as shown in Figure 7. After irradiation, the thin film is removed from the detector so the etchant can react with tracks in the detector. Registration marks are used to locate fuel particles on the thin film relative to fission track stars found on the etched detector. Lee et. al showed submicron particle control and improved error of enrichment analysis by separating submicron particles of different enrichment [17]. Dizgala et. al recently reported an easily repeatable method for particle control and semi automatous particle analysis in an IAEA laboratory [9].

**Table 1. List of measured critical angles for various etchable SSNTD for $^{252}$Cf SF fragments and $^{235}$U thermal neutron induced fission fragments. Efficiencies assume a $2\pi$ geometry.**

| Detector | $^{252}$Cf $\theta_c$ | $^{235}$U $\theta_c$ | $^{252}$Cf $\varepsilon$ | $^{235}$U $\varepsilon$ |
|---|---|---|---|---|
| Muscovite Mica | 4°30' [a] | 3°41' [b] | 91.8% [a] | 93.6 ± 0.3% [b] |
| Phosphate Glass | | 7°06' [b] | | |
| Silicate Glass | | 37°21' [b] | | |
| Quartz | | 16°02' [b] | | |
| Polycarbonate | | 2°24' [b] | | 27% - 64%[c] |
| Makrofol Polycarbonate | 3°00' [a] | 4°30' [b] | | |
| Makrofol K Polycarbonate | | 3°40' [b] | | |
| Polyester | | 3°29' [b] | | |
| Soda-Lime Glass | 35°30' [a] | | | 39.3 ± 0.4% [b] |
| U2 Reference Glass | 31°45' [a] | | | |
| Obsidian | 26°00' [a] | | | |
| Tektite | 25°45' [a] | | | |
| Lexan Polycarbonate | 2°31' [a] | | | |

[a] [18]
[b] [13]
[c] [10] Report compares fission track counts to SIMS analysis.

## Thermally Stimulated Luminescent Detectors

Thermal stimulated luminesce (TSL) detectors or thermal luminesce dosimetry (TLD) badges are commonly used in occupational dosimetry and medical treatment monitoring [19], [20]. TLDs are passive radiation detectors that store information in the form of latent amorphous damage. Upon heating, the detectors anneal releasing photons with intensities and energies that are directly

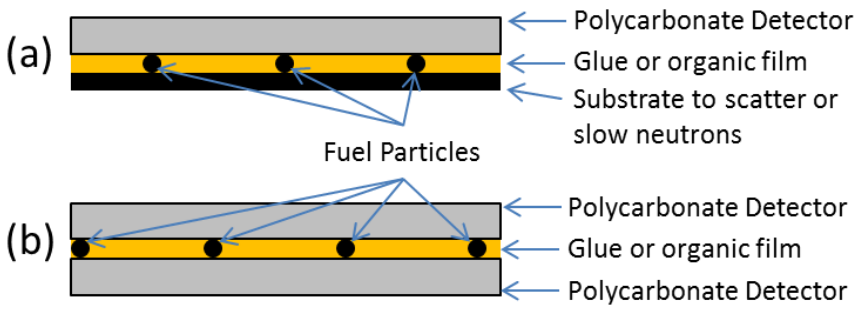



**Figure 7. (a) is a typical configuration of a single sided polycarbonate SSNTD and (b) is a typical configuration of a two sided polycarbonate SSNTD.**

related to the radiation exposure seen by the detector. An example of a LiF TLD glow curve is shown in Figure 8 with amorphous structures releasing photons dependent on temperature and atomic mobility at depth within the solid. By selecting materials sensitivity to particular radiation types and energies, complex fields may be characterized with TLDs. Additionally, masking materials are often used to block particular types of radiation like betas with aluminum or create secondary radiation to which the detector is sensitivity, like neutron detection using protons from $^{6}Li(n,\alpha)^{3}H$. TLDs are important to understand as they share a number of characteristics with optically stimulated luminesce detectors (OSLD).

TLDs are useful in a broad range of environments from uGy to MGy exhibiting linear and superlinear responses. The intensity's relationship to dose when well below saturation is described by

$$I = \frac{(\alpha D)^2 N(a+1)}{a+\alpha D} \quad 4,$$

where I is the luminescent intensity [arb. units], $\alpha$ is a scalar described by the relationship between the LET and luminescence, a is the background intensity, D is dose [Gy], N is physical constant of the detector, and when $\alpha D \ll a$ intensity grows quadratically with dose [21].

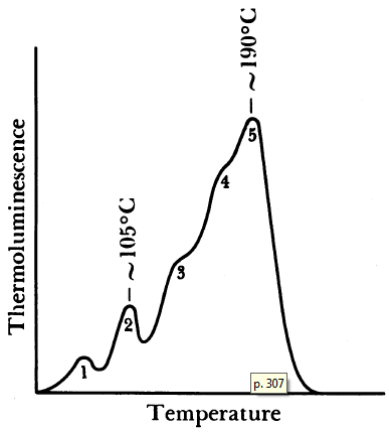



**Figure 8. The glow curve for LiF:Mg,Ti. Numbered peaks represent different trap depths and different defect types. For most TLDs, multiple glow peaks are present and dopants can shifted peaks and also may improve peak resolution [22].**

However, TLDs are limited to bulk radiation detection and do not have single ion or point defect detection resolution. For this reason and others, OSLD research has seen an increase in developmental effort since it has been shown to reliably produce single particle latent track resolution.

## Optically Stimulated Luminesce

Optically stimulated luminescent detectors (OSLDs) are similar to TLDs in that they store radiation damage in latent amorphous structures [23]. However instead of thermally induced relaxation, the amorphous structure, commonly called color centers in OSLDs, are excited photonically and the subsequent de-

excitation is characterized by a Stokes or occasionally anti-Stokes shift. While annealing may occur during this process, it has been shown that this excitation/de-excitation can result in stable or possibly semi-stable defect blinking [24]. When annealing occurs as a result of photonic excitation, it is referred to as bleaching. Therefore depending on a color center's stability, information stored in OSLDs may be collected multiple times before information is lost or degraded [25], [26].

Like TLDs, OSLDs are suitable for a wide range of doses but additionally have high spatial resolution. Ten years of research into OSL has led to number of options currently available for OSLDs providing various sensitivities and resolutions. Some options that provide good sensitivity to ionizing radiation are $MgO:Tb_3^+$; $Al_2O_3$:C; $Al_2O_3$:C,Mg; $CaB_6O_{10}$:Ce,LiCl; and now LiF [27]–[29]. However, single track analysis is only currently researched in $Al_2O_3$:C,Mg and LiF, with fantastic results using $Al_2O_3$:C,Mg showing secondary delta rays and 'on cell' or single cell dosimetry [7], [30]–[32]. Single track resolution is superior in these mediums and intensity of color centers is sufficient for detection, however improvements are still needed in signal to noise ratio (SNR) for LiF.

A variety of detector features are important to understanding how OSLDs work. It is necessary to consider pathways in which ionizing and nonionizing radiation change the molecular structure of the detector, the types of fluorescing defects, excitation energies, de-excitation period, band gaps structure, thermal stability of defects; and sensitivity to other forms of radiation particularly neutrons as they can activate the detector or induce fission and may reduce the SNR.

For precision measurement, OSLDs are highly desirable over TSL and etchable fission track detection methods. OSLDs require few sets for analysis and require less rigorous particle control. Efficiencies are already comparable to modern track detectors. Using low fluences of carbon ions Osinga et al. reported 99.83% particle detection efficiency in Al2O3:C,Mg [33]. While the ideal conditions under which this sample was irradiated are not possible with

nondestructive measuring of fuel particles, a well-prepared sample should achieve near 100% efficiency.

## Lithium Fluoride

Lithium fluoride is a well characterized material for nuclear track detection for both chemical etching and fluorescing excitation [34], [35]. Heavy ion damage abundantly generates fluorescing color centers. The Frenkel defect (F-type) is particularly relevant in room temperature OSL both in its first order, a single defect, and it's more complex form with cluster of adjacent defects in various local charge states. A Frenkel defect is a displacement of an ion from its normal sub lattice position into an interstitial site. The displaced ion and vacancy of a F-type defect in LiF requires no less than 2-3 lattice spacing (approximately 0.8-1.2 nm) to remain stable [34]. The defect's vacancy necessarily creates a local net positive charge and is often occupied by an electron. In the case of LiF, the fluorine sub lattice forms defects called F-band, F-type, or F-center. A small sample of defects are illustrated in Figure 11. The H-center or $v_K$-center defects are more common with Schottky defects where vacancy in an anion sub lattice is not filled by an electron due to cationic isolation.

For this study, visible light (VIS) is preferred and LiF's $F_2$, $F_3^+$, and $F_4$-like (overlapping with Li collide) have excitation and emission spectra between 450 nm and 800 nm making it suitable.[3] The formation of these preferred F-type defects is dependent on radiation type and energy, and the temperature during and after irradiation. LiF optical density after irradiation is presented in Figure 9 showing the relationship between optical density and excitation wavelength adsorption, and defect creation dependency on radiation type. Fortunately for this work, $F_2$ and $F_3^+$ excitation overlap with peaks very close to 450 nm. Behavior of defect formation is very temperature sensitivity; however, room temperature experiments are primarily important to this work. Baldacchini et al. compiled a

[3] A $F_2$ defect is two adjacent fluorine vacancies, each filled with an electron. A $F_3^+$ defect is three adjacent fluorine vacancies with only two filled with electrons. A $F_4$-like defect is four adjacent fluorine vacancies, each filled with an electron.

convenient list of temperature dependency and other optical parameters for various defects [36]. Figure 10 shows temperature dependence $F_2$ and $F_3^+$, and their excitation overlap. Fortunately, the Stokes shift of each defect allows two distinctly resolvable emission peaks. From Figure 11 it is seen that reduced temperatures enhance $F_3^+$ defects. The lower temperature impact on defect behavior is understood as the result of reduced ionic mobility following the columbic explosion (CE) event of the ion entering the crystal irradiation leading to 'freezing' of higher order defects.

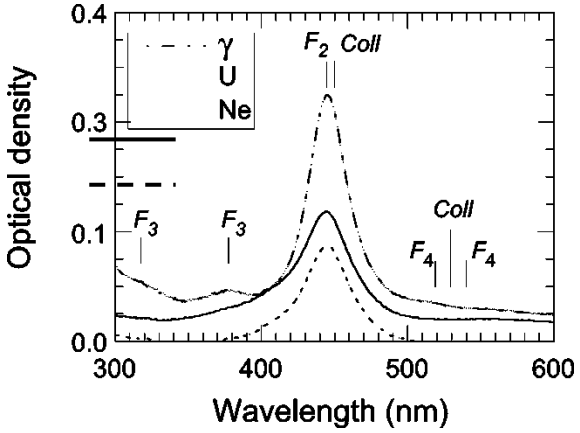



**Figure 9. Absorption spectra for LiF irradiated with 275 kGy $\gamma$-ray, 750 kGy 31 MeV Ne ions ($5x10^{11}$ $cm^{-2}$), and 150 Gy 1400 MeV U ions ($10^{10}$ $cm^{-2}$). The band positions of different color centers and colloids are indicated. The $F_3$ and $F_4$ bands are clearly separated from the $F_2$ band for $\gamma$ exposure, however ion beams induce broadening from 350–500 nm region [37].**

A variety of LiF's normal physical properties are important to understand when explaining fluorescence behavior and are required for calculations and models completed in this study. Table 2 tabulates these properties. LiF's high transparency in the visible range and refractive index similar to water and immersion oils makes it a suitable candidate for fluorescing microscopy. Figure 12 is the room temperature transmission spectra for LiF used in this study and clearly shows an expected transmission of greater than 90% for $F_2$, $F_3^+$, and $F_4$-like excitation and de-excitation energies. LiF's density results in preferred ion

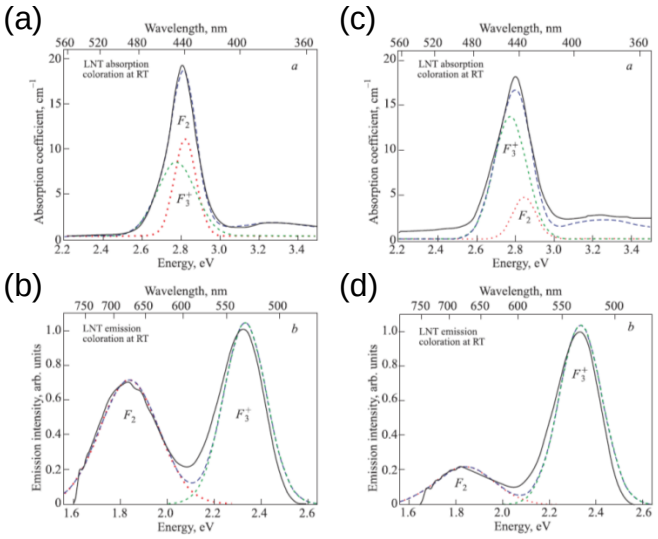



**Figure 10. Compares excitation and emission dependences on temperature for LiF irradiated with 3 MeV electrons. Inspections occurred at 77 K. Absorption or emission coefficients are solid lines and best-fit (Gaussian) curves are dashed lines. For (a) and (b) irradiation occurred at room temperature (RT) with $4.5 \times 10^4$ Gy. (b) the photoluminescence spectra was excited at 457.9 nm. For (c) and (d) irradiation occurred at 213 K with $1.6 \times 10^5$ Gy. (d) the photoluminescence spectra was excited at 457.9 nm. $F_3^+$ to $F_2$ creation is inversely dependent on temperature [38].**

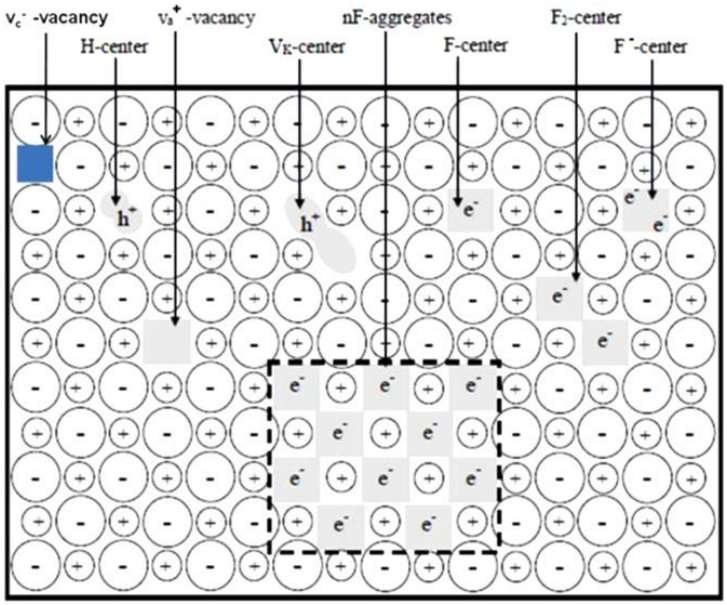



**Figure 11. Various defect structures found in LiF [39].**

**Table 2. LiF physical property values used for calculations and design of experiments.**

| LiF | Value |
|---|---|
| Lattice Constant [nm] [a] | 0.4026 |
| Cleavage plane [a] | <100> |
| Transparency Range [nm] [a] | 110~7000 |
| Constant of Thermal Dispersion [dn/dT] [per °C and 1.1 μm] [a] | $-1.50 \times 10^{-5}$ |
| Melting Point [°C] [a] | 870 |
| $F_2$ and $F_3^+$ Thermal Stability Point [°C] [a] | 410 |
| Linear Coefficient of Thermal Expansion [per °C] [a] | $18.9 \times 10^{-6}$ |
| Refractive Indices [a] | 1.39 at 1um<br>1.30 at 6um |
| Density [g/cm$^3$] [a] | 2.639 |
| Knoop Hardness [a] | 99.1 |
| Young's Modulus [GPa] [a] | 64.97 |
| Shear Modulus [GPa] [a] | 55.14 |
| Plasmon energy [eV] [b] | 25 |
| Exciton energy[eV] | 12.9[b], 13.5[b] |
| Valence band Width [eV] [b] | 6.1 |
| Static dielectric constant [b] | 9.27, 8.90 |
| Optic dielectric constant [b] | 1.92, 1.90 |
| $F_2$ decay time [ns] [c] | 15.5 ± 0.8 |
| $F_3^+$ decay time [ns] [c] | 8.1 ± 1.2 |
| Solubility in Water, at 25 °C | 0.134 g/100 mL |

[a] [40]
[b] [41]
[e] [36]

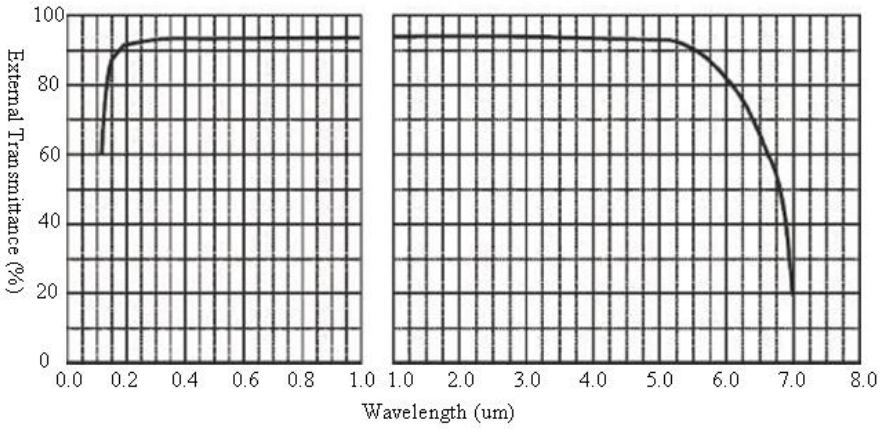



**Figure 12. External Transmittance curve for Lithium Fluoride Crystals as per the material vendor [40].**

travel ranges and resolvable linear energy transfer (LET) profiles from ions close to fission energies. Its linear coefficient of thermal expansion makes it able to support the induced heat load of higher irradiation intensities. The moduli and hardness indicate the crystal will preserve latent tracks even after sustaining cleaving damage. Cleaving damage was common as the crystals were 12.7 mm by 0.5 mm discs and brittle. LiF's dielectric properties make it an insulator which is required for standard SSNTDs, however semiconductors can be used in specific applications of LETs >10 keV $nm^{-1}$. Short decay times of $F_2$ and $F_3^+$ allows higher speeds when using rastering collection tools and by definition means the light response observed from these defects is fluorescence. LiF has a low solubility in water but will result in the destruction of possibly useful amorphous structures in and around ion tracks in a few hours. Furthermore, water immersion microscopy is necessary in particular applications due to its beneficially long working distance (WD). Fortunately, optical substitution gels are available with refractive indices similar to water and are further discussed in Chapter IV.

OSL is sensitive to impurities in crystals. Dopants are commonly used to modify crystal performance or in some cases completely change behavior. Therefore, it is important to understand the purity of LiF used in this work. Table

3 lists the known impurities in LiF crystals used in this study. While less than 10 ppm of any one impurity is desired, Cl has no known impact on OSL proprieties of irradiated LiF. Additionally, latent tracks are observed. If in ultra-high purity LiF track behavior changes, then impurities listed here may be investigated for performance altering dopant effects.

**Table 3. List of reported impurities in single LiF crystals used in this work. Crystals have a nominal mass of 167.2 mg. Values evaluated and reported by Precision Micro-Optics Inc.**

| Constituent | Concentration [ppm] |
|---|---|
| LiF | 999900 |
| Cl | 50 |
| $SO_4$ | 2 |
| OH [mmol/g] | 2.5 |
| Fe | 4 |
| $SiO_2$ | 2 |
| H [mmol/g] | 5 |
| Heavy Metal (e.g. Pb) | 4 |
| Others | 30 |

A number of models have been used over the history of irradiated materials to describe MeV ion collision with detectors. The current prevailing explanation is the CE model [37]. This model describes the rapid penetration of a highly charged ion into a solid, in this case LiF. The ion quickly ionizes a majority or all of atoms in its local vicinity (e.g. <25 atoms perpendicular to the direction of travel) causing a sudden large local net positive charge in the crystal. The ionized Li and F repel one another causing an explosive like event which leaves behind a highly amorphous structure.

The nuclear properties of lithium isotopes in neutron fields must be considered in addition to the physical properties. Because of the relatively high fission cross-section of $^6$Li which occurs naturally at 7.6% and releases 4.8 MeV by thermal neutron fissions in

$$^{6}_{3}Li + ^{1}_{0}n \rightarrow ^{4}_{2}He + ^{3}_{1}H \quad 5.$$

This reaction produces local ion tracks within LiF. Fortunately, these ions have very low LET's and are no visible using current OSL methods. Moreover, observed tracks from this reaction would originate isotopically throughout the crystal and should be distinguishable from tracks entering from the surface of the crystal.

Overall LiF is an excellent candidate for a FNTD. It was selected for these reasons and because of it well characterized optical properties under irradiation. Based on the properties listed above and experience with LiF, other highly desirable properties not found in LiF, like castability and characterized ion collision luminescence, are discussed in Chapter VIII.

This work only used optical grade single crystal LiF. Discussed in Chapter IV, early work showed significant $F_2$ and $F_3^+$ background on the surface of single crystals suggesting that polycrystalline structure would not have a suitable SNR for track detection; however refined annealing pretreatments resulted in significant improvement in background reduction. This development opens the possibility of polycrystalline use but was not pursued as part of this work.

## Confocal Laser Scanning Microscope

Confocal Laser Scanning (fluorescing) Microscopy (CLSM) is a technique that involves using specific energies of light to excite fluorescing response(s) from a target while controlling the excited and crucially, observed volume. The fundamental characteristics of a confocal microscope are shown in Figure 13. This study used a Lecia TCS SP8 inverted CLSM.[4] A diagram of the system in an upright configuration is illustrated in Figure 14 and the system used for this work during operation is shown in Figure 15. The microscope was operated in both

[4] Additional information about the Leica TCS SP8 is found on the Leica Microsystems Homepage or at http://www.leica-microsystems.com/products/confocal-microscopes/details/product/leica-tcs-sp8/.

normal and resonance mode. CLSM most important feature in application for this work is submicron resolution of extremely low light sources. By understanding confocal light microscopy's physical limits, limitations can be assigned to parameters in OSL fission track analysis. Recent work by Neuholz et al. describes some of these parameters where high areal track density and large single image (large angle) exposures are limited to two-digit percentage fluence uncertainty for Spread-out Bragg Peak [42].

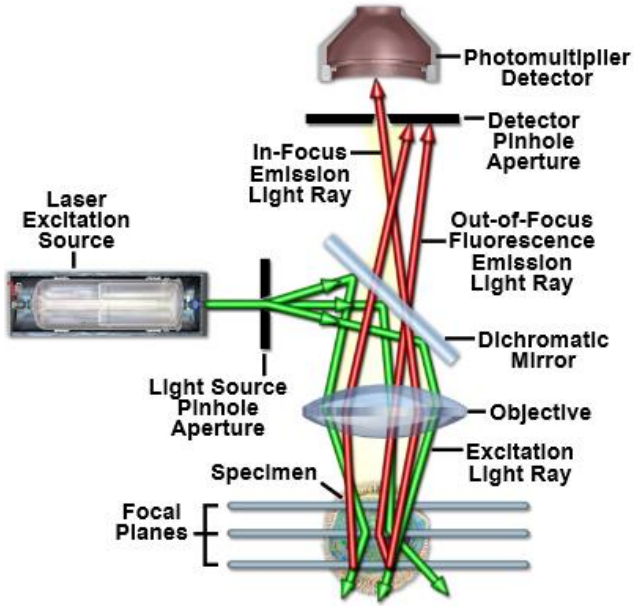



**Figure 13. Diagram of the light path of a confocal microscope. Light travels bi-directionally though the objective with adjustable focal planes allowing the microscope to bring various layers within the working distance of the objective into focus. The pinhole aperture in front of the detector, the focal distance, and the wavelength of fluorescing light define a raw collection voxel's dimensions [43].**

### *Excitation, Emission, and Resolution*

Two areas of CLSM must be understood to realize the capabilities and limitations that affect this tool when investigating fluorescing samples: light

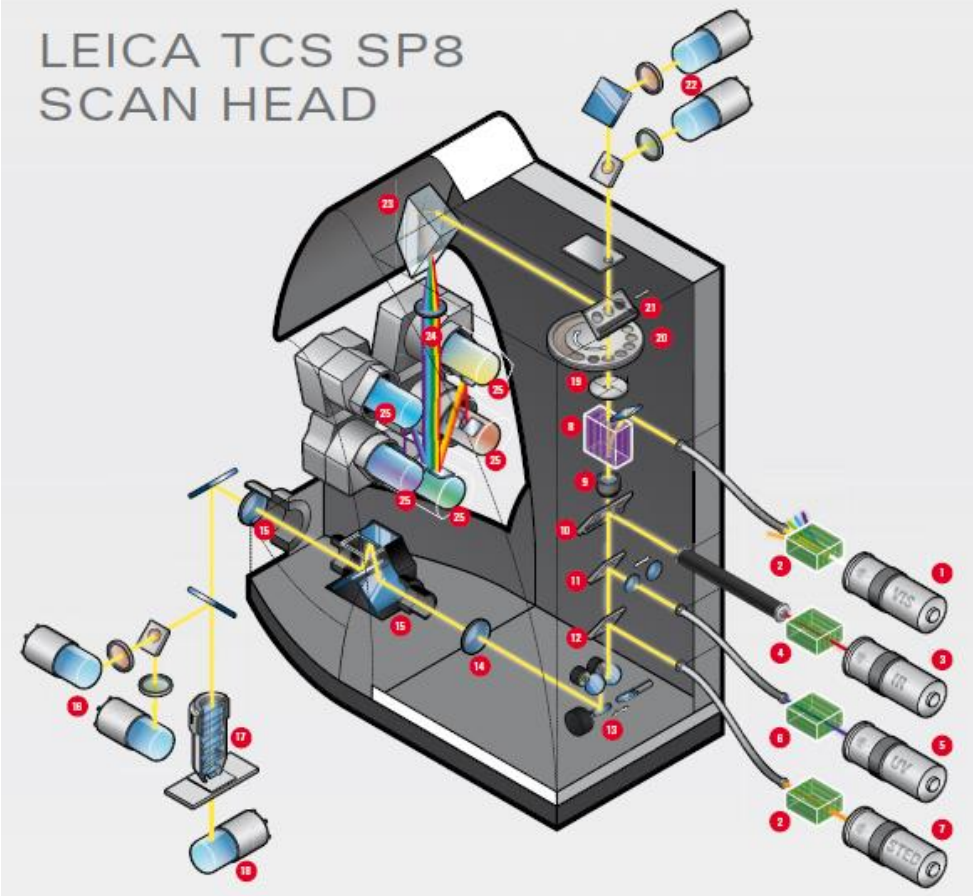



**Figure 14. Diagram of an annotated upright Lecia TCS SP8 CLSM. The system used for this work is inverted variant of the diagramed microscope. Components listed in the diagram are the following: (1) White light laser (WLL), (2) Acousto-optical tunable filter, (3) Infrared Laser*, (4) Electro-optical modulation*, (5) Ultraviolet laser (UV), (6) Direct Modulation*, (7) STED laser*, (8) Acousto-optical beam splitter*, (9) FRAP Booster, (10) IR laser incoupling*, (11) UV laser incoupling CS2 UV optics, (12) STED laser incoupling*, (13) FOV Scanner with Tandem Scanner, (14) Scan optics with alternative UVIS, HIVIS, VISIR coating, (15) Scan field rotation (Abbe-König rotator), (16) Reflected light detection PMT in non-descanned position*, (17) Objective lens, (18) Transmitted light detection PMT in non-descanned position, (19) Square confocal pinhole, (20) Fluorifer disc, (21) Outcoupling with X1 port, (22) External detection*, (23) Prism-based dispersion, (24) SP detector with spectrophotometer arrangement, and (25) Two photo-multipliers (PMTs) and three hybrid photo detectors (HyD) [44].**

*** denotes features not present on the system used for this work**

control and spatial resolution. Near-ultraviolet (UV) and visible (VIS) lasers are able to excite fluorescing centers while visible light detectors are able to collect reflected, transmitted, and fluorescing light. The confocal aperture and scanning head control light collection isolating the detector from light arriving outside of the desired voxel. These physical controls are optimized so voxel dimensions approach the theoretical resolution allowed by Rayleigh's limit.

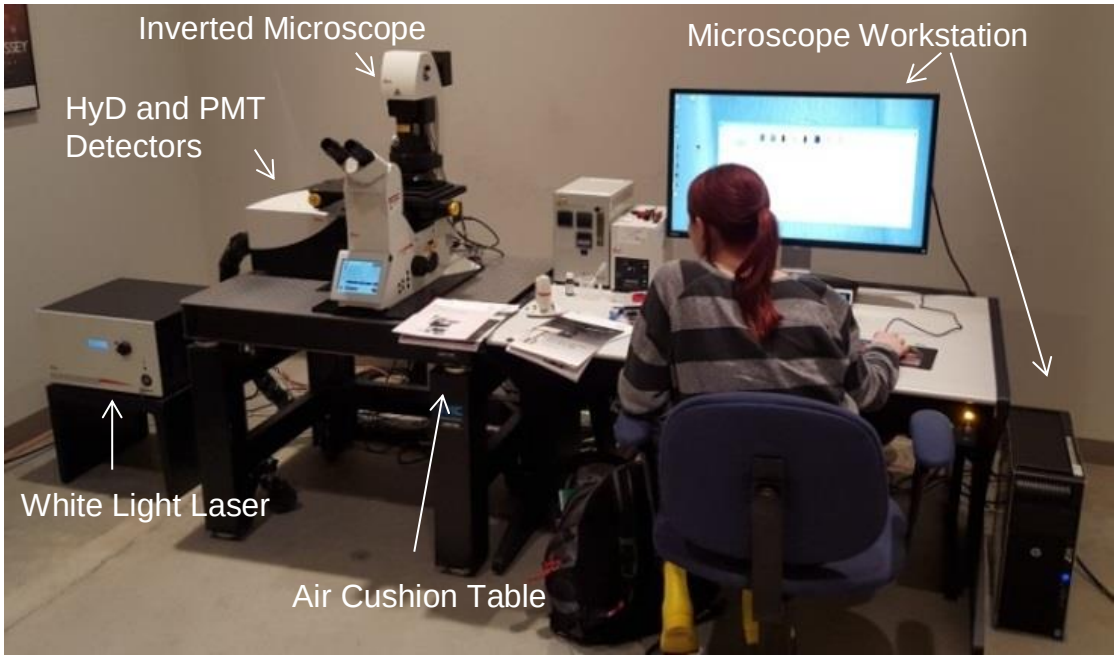



**Figure 15. Picture of Lecia TCS SP8 CLSM used for this work at the University of Tennessee Advanced Microscopy and Imaging Center.**

Three lasers are available on this microscope: a 405 near-UV diode laser, an argon laser with 5 lines, and a white light laser (WLL). They provide excitation lines for most of the visible spectrum from 405 to 750 nm. The detectors used in this study have room temperature stable color centers that are activated with the argon laser and WLL. The lasers were each set at a nominal output of 14-16 mW in continuous wave (CW) mode. Laser power control is important since many fluorescing sites bleach and for long working distances diffraction degrades performance. This system provides settings for programmed or manual scaling of

laser intensity based on z-depth, duration of scan, and sequential scan programming. These features of the excitation light allow for qualitative optimization and quantitative control of fluorescing sites.

Light collection is accomplished with standard photo multiplier tubes (PMT) for moderate to high intensity sources and with hybrid (HyD) PMT/avalanche diode collectors (AVD) for low to moderate intensity light sources [45]. PMTs were used for reflection images and HyDs were used for all latent track images. The HyD's GaAsP cathode has a 45% quantum efficiency at 500 nm and a true single photon minimum limit of detection (MDL) per voxel (at maximum resolution ~0.015 $\mu m^3$). In count mode, the gain is 10 V in order to improve SNR from low light sources; however, the HyD is capable of up to 400 V of logarithmic multiplication. The HyD's specialized avalanche-like setup is shown in Figure 16. The detector surface of the HyD is also smaller than the PMT allowing for less 'dark current' or background electronic noise natural produced naturally by operating the detector. Time gating is available on this device to block reflection or isolate specific emission delays; however, it is was not necessary for the color centers used in this work as the Stokes shifts of all materials used are >80 nm (>0.26 eV). In addition to these parameters enabling imaging of low light latent ion tracks in LiF, these parameters are appropriate for rapid scanning microscopy (resonance mode).

Spatial resolutions are limited by the point spread function (PSF), illustrated only for the focal plane in Figure 17. The spread results from the complex nature of light diffraction about the zero-dimension theoretical focal point of an objective. For light microscopy below UV energies, this spread is directly due to incoherent scattering on electrons in the illuminated region. These complex interactions are aggregated into an analytical description dependent on wavelength and characteristics of refractive layer variance (physical microscope parameters and sample characteristics).

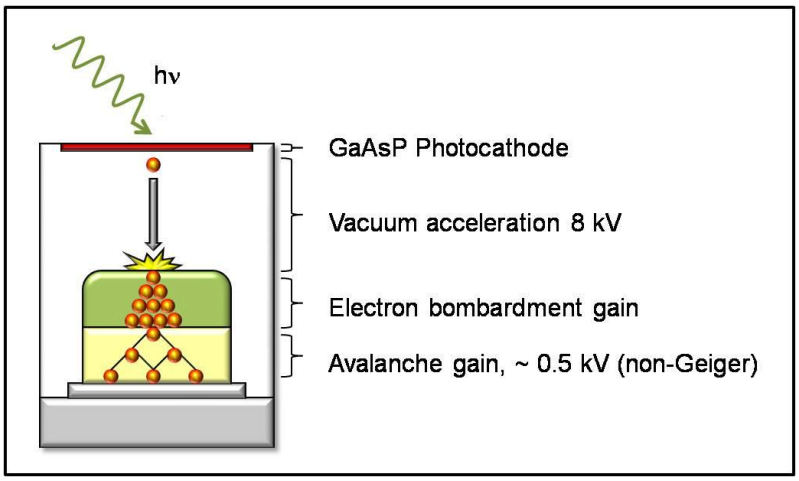



**Figure 16. A basic schematic of the HyD [45]. Due to the vacuum region and the semiconducting electron gain region the photon efficiency is very close to the quantum efficiency of the cathode. Additionally, the straight line relationship between the cathode and the semiconductor means that the pulse width is minimized and time gating can reasonable achieve nanosecond resolution.**

The lateral resolution parameters [nm] are defined by the PSF,

$$\boldsymbol{R_{x,y}} = \frac{\boldsymbol{hv}}{\boldsymbol{2NA}} \qquad 6,$$

where $hv$ is the wavelength of the light passing through the objective [nm] and the NA is the optimal condition where the refractive index between the objective and the focal point does not change. This means that lateral resolution is generally restricted to half of the wavelength used for inspection as originally observed by Hooke 1672.

The axial resolution is also defined by the PSF,

$$\boldsymbol{R_z} = \frac{\boldsymbol{2hv}}{\boldsymbol{NA^2}} \qquad 7$$

where notably the performance limit is much more dependent on numerical aperture and is dependent on twice the wavelength. Therefore, axial resolution is typically less than lateral resolution.

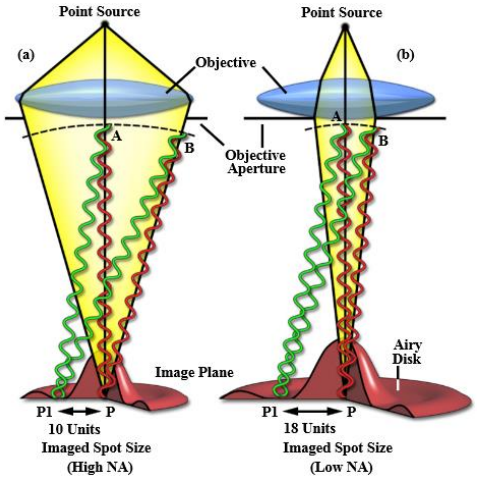



**Figure 17. The PSF is illustrated by two different objective diameters. In (a), the large objective diameter results in a large angle of light from the focal point which is defined as a high NA. In (b), the objective diameter is small resulting in a smaller angle of light from the focal point, therefore a lower NA. Also, the airy disc is more recognizable in (b) since a lower NA means a large airy [46].**

Expectations to the diffraction limit with light microscopy techniques. Particularly useful is fluorescing microscopy where two or more photons are used in a non-linear manner to excite color centers. This technique has the potential to reduce noise, de-convolve overlapping fluorescence, and improve resolution to nanometers.

In the TCS SP8, excitation light is emitted via a rastering laser that scans across the image area and is collected through one of five objectives listed in Table 4, with their respective resolutions limits. The aperture effectively masks a ring around the outer edge of the objective lens. All reported work uses either the 40x water, 40x oil, or most often, the 63x.

### *Inverted Sample Setup*

The inverted microscope setup requires a change to typical sample preparation for immersion microscopy. Samples are still viewed through a coverslip however; the coverslip replaces the glass slide as the samples' substrate. Due to the short working distances of the high NA objectives, a 1.5 thickness (160 μm) coverslip must be used to bring the sample into focus. Figure 18 shows the normal light path for a typical sample. When tracks are on surface A in Figure 18, immersion media and a coverslip or second crystal must be placed above surface A to prevent diffraction and refraction from obscuring fluorescence near surface A.

**Table 4. A list of objectives and associated parameters available on this the TCS SP8 CLSM. Numerical aperture (NA) is a dimensionless number that describes the range of angles over which the objective can collect light. NA is therefore closely related to the working distance (WD) by NA = WD/objective diameter. All objectives are in-line with a built-in 10x lens on the microscope. Best resolutions are evaluated for 488 nm light.**

| Objective (10x built-in lens) | Immersion (Refractive Index) | NA | Working Distance [μm] | Best XY Resolution [nm] | Best Z Resolution [nm] |
|---|---|---|---|---|---|
| 10x | Air (1.000) | 0.3 | 11000 | 651 | 4768 |
| 25x | Water (1.333) | 0.95 | 2400 | 206 | 551 |
| 40x | Water (1.333) | 1.1 | 650 | 178 | 378 |
| 40x | Oil (1.518) | 1.3 | 240 | 151 | 300 |
| 63x | Oil (1.518) | 1.4 | 140 | 140 | 236 |

### *Sampling Parameters*

Three sampling parameters require explanation to understand their limiting effects and how they can be optimized in application to FNTDs. The parameters allow for image enhancement, substantial scanning speed increases, and improvement of SNR. All three were implemented and refined during this work in application to FNTDs.

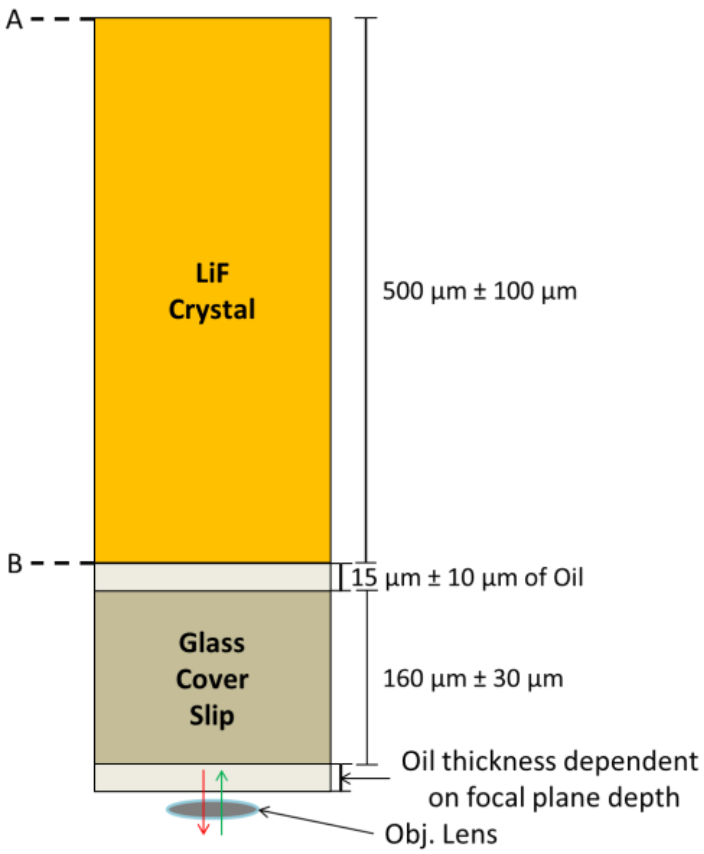



**Figure 18. A diagram of the light path through a typical sample. The green and red lines are excitation and emission light directions, respectively. The objective lens is immersed in oil. Layers with dimensions are to scale. The region of interest is typically surface B however, when using longer working distances surface A can be investigated.**

First, oversampling convolves voxels so that sub diffraction limit images can be rendered. In combination with linear interpolation, the TCS SP8 can present lateral voxel dimensions down to 10 pm, however the highest magnification (63x) at minimum digital zoom is optimized for lateral dimensions of 66 nm at ≤600 Hz voxel scan speed. An additional challenge with ultra-high-resolution oversampling renders is the file size, which quickly exceeds 2-4 Gb requiring more 6 hours per stack to scan. Most importantly, very small voxels lose quantitative value and qualitative results are not improved beyond optimized settings. For these reasons, optimized oversampling is used for a majority of this work. These settings produce 130 nm x 130 nm x 900 nm raw collection voxels and collection shifts laterally 66 nm and axially 300 nm to oversample. This 2-3 times oversampling convolves into images with 66 nm x 66 nm x 300 nm voxels.

Second, lines and images are scanned multiple times and then voxel intensities are added or averaged. This can improve SNR when adding or smooth out fluorescence instability; however due to the extremely low light environment of only a few photons per voxel per dwell, a significant variance in intensity occurs due to quantum efficiencies in primarily, fluorescing sites and the HyD detector. This variance was replicated with different dwell times and with fluorescing standards that have similar excitation and emission spectra. This variance is discussed more in Chapters III & IV since it significantly impacts the repeatability and error when analyzing the track intensity as a function of depth.

Third, the TSC SP8 can operate in a ‘resonance’ mode, where switchable galvanometric mirrors enable 8000 Hz voxel scan speeds reducing scan times by 20 to 40 over typically high-resolution scanning using 200 to 400 Hz. Necessarily, voxel dwell times are equally reduced. For low light sources, increased excitation laser intensity is necessarily to maintain reliable signal. Additional at 8000 Hz, dwell time may drop below 50 ns. Dwell times must be long enough for excitation and emission to occur. In LiF for this work, $F_2$ and $F_3^+$ decay times are known 8.1 ± 1.2 and 15.5 ± 0.8 ns, respectively [47]. If dwell time is lower than 16 ns then excited electrons will not have enough time to decay; however due to

oversampling, signal may be collected down to approximately 11 ns of dwell time but is not preferred due to a loss of 33% fluorescing intensity. This is readily managed by limiting the resolution of images in resonance mode to no less than the optimized resolution values which use a dwell time of 35 ns.

## Nuclear Physics Modeling Codes

### *MCNP*

Heavy ion physics is a complex nonlinear, energy regime dependent behavior. Computer modeling provides a relatively fast, accurate approach to predicting ion behavior under a wide range of conditions. General Monte Carlo N-Particle (MCNP) Transport Code provides geometry dependent physics modeling of neutron transport and heavily ion physics in the energy regimes appropriate for this work [48]. Modeling uses a variety of theoretical and empirical parameters and fits to predict behavior. The code is particularly suited for modeling neutron induced fission. MCNP v6.1 was used for this work and additional detailed information is available at the program's Los Alamos homepage including the user's manual.[5] MCNP's application is further discussed in Chapter IV.

### *SRIM*

The Stopping and Range of Ions in Matter (SRIM) was used for simple ion transport and irradiated materials modeling [49].[6] This set of programs is based on nuclear collision modeling and the Bethe-Bloch equation but extend much farther than other analytical solutions with fitting parameters as necessary. In the subprogram TRIM, numerical Monte Carlo transport is applied providing a graphical representation of ion attenuation behavior throughout a two-dimensional environment. SRIM provides estimates for ion range in various materials with the ability to build new materials from manual stoichiometric input.

[5] Further information on the latest version of MCNP is found at https://mcnp.lanl.gov/, last verified access on 6 May 2017.
[6] Further information on the latest version of SRIM is found at http://www.srim.org/, last verified access on 6 May 2017.

The continuous slowing down approximation (CSDA) is one of the analytical tools used for heavy ion behavior modeling in SRIM. This approximation is particularly useful in the energy regime used for fission ions in track detectors. The CSDA is an excellent analytical tool for understanding relevant factors in slowing down ions. The relevant factors when predicting ion deceleration are ion energy, ion charge, ion mass, and target electron density.

# CHAPTER III: ALPHA TRACKS

Alpha particles are helium ions commonly produced by natural decay from heavy elements including many actinides. For investigation, $^{241}$Am and isotopes of Cf were used to create alpha tracks. They are excellent sources for both gross alpha counting and alpha spectroscopy since their activities and alpha decay spectrums are similar to U and Pu. Additionally, $^{241}$Am and Cf have well characterized decay yields and spectra. The median and peak LETs for alphas are very low compared to fission produces, occurring at 4-6 MeV for $^{241}$Am and Cf [50]. Since defects from irradiation are heavily dependent on linear energy transfer, alphas generate significantly less defects than that of fission products. Alphas abundance and natural occurrence makes detection, and if possible spectral analysis, highly desirable to aide in characterizing fissile materials.

Latent $F_2$ and $F_3^+$ tracks caused by alpha radiation are identified in LiF from $^{241}$Am and a mixed isotope Cf sources. Bilski et. al made the first observation of latent $F_2$ and $F_3^+$ tracks from $^{241}$Am alpha radiation in LiF [31]. The findings mentioned in this Chapter and discussed in Chapter IV are the first reported identification latent $F_2$ and $F_3^+$ alpha tracks from Cf. Tracks are analyzed for LET dependent behavior including, intensity and track length.

## Alpha Sources

A plated 10 μCi $^{241}$Am alpha source was used in basic experiments because of its relative ease of handling and availability. Alphas from $^{241}$Am have between 4.800 and 5.545 MeV energies with majorities at 5.486 MeV (86%), 5.443 MeV (12.7%), and 5.389 MeV (1.3%) [50]. In SRIM models of $^{241}$Am, 5.45 MeV is used as the alpha total kinetic energy (TKE) upon contact with the detector face. For a 5.45 MeV unattenuated alpha impinging on the surface of a LiF single crystal, the peak LET is predicted to be 0.408 keV nm$^{-1}$ at approximately 18.5 μm from the surface. Alphas are expected to attenuate to 10 keV TKE after traveling 20.8 μm in the LiF, after which ion behavior is expected to drop below the limit of detection. This limit of detection is based on the point at

which an ion's behavior becomes dominated by the effects of the Frank-Condon Principle.

A mixed Cf source was used for alpha track investigation. The first identification of alphas tracks was observed with this source allowing for in-situ benchmarking with fission tracks. Two experimental series were completed with the Cf source. Once with an activity of 340 μCi and approximately one year later with an activity of 260 μCi. The major alpha contributors from the mixed Cf source are $^{249}$Cf, $^{250}$Cf, $^{251}$Cf, and $^{252}$Cf. Cm daughters grow into the source without equilibrium ($t_{1/2}^{p} < t_{1/2}^{d}$) and decay primarily by alpha. However, Cm alpha activity is significantly lower than Cf and, therefore, contributes <0.004% to the alpha population. Table 5 lists the normalized alpha activity in the source by Cf isotope, alpha energy ranges, and major alpha energies by abundance. Table 5 shows that >80% of alphas produced from the source begin with energies just over 6 MeV. For this reason, SRIM models of Cf alphas use 6 MeV for ions striking the detector face. For an unattenuated Cf alpha in LiF, the peak LET is predicted as 0.408 keV/nm at 21.7 μm from the surface. Alphas are expected to attenuate to 10 keV TKE after traveling 23.9 μm.

## Experimental Method

Two experimental methods were used to obtain alpha tracks in LiF: one using the plated 10 μCi $^{241}$Am alpha source, and the other using the plated Cf source. Exposures and examination using the $^{241}$Am source were completed at the University of Tennessee. Exposures using the Cf source were completed at the Lynchburg Technology Center (LTC), BWX Technologies Inc. Examinations of Cf exposed LiF were completed at the University of Tennessee.

Optical LiF single crystals were obtained from PMOptics Inc. Crystals were 12.7 mm by 0.5 mm right cylinders polished to a 1 μm finish on both radial faces. Initially, crystals were not thermally pretreated. It was discovered that polishing left significant $F_2$ and $F_3^+$ defects along the surface of the crystals contributing substantially to background. Crystals were later thermally pretreated

by heating to 450°C for 20-30 minutes to reduce remove most background. Crystals were periodically analyzed and verified to have reduced background fluorescence.

**Table 5. A list of isotopic quantities and known alpha decay energies for alpha radiation contributors in the electroplated Cf source.**

| Isotope | 1st Exposure Normalized Alpha Activity / 2nd Exposure Normalized Alpha Activity | Alpha Energy Range [MeV] | Primary Abundances of Alpha Energies [MeV (Abundance %)] |
|---|---|---|---|
| $^{249}$Cf | 0.295% / 2x10$^{-6}$% | 5.201-6.194 | 5.8120 (84.4), 5.9462 (4.00), 5.7597 (3.66), 5.9034 (2.79), 6.1940 (2.17), 6.1395 (1.11), 5.8495 (1.04) |
| $^{250}$Cf | 12.587% / 15.111% | 5.738-6.0308 | 6.0308 (84.7), 5.9891 (15.0) |
| $^{251}$Cf | 0.072% / 0.091% | 5.501-6.074 | 5.677 (35), 5.852 (27), 6.014 (11.65), 5.632 (4.5), 5.8144 (4.2), 5.762 (3.8), 5.648 (3.5), 6.074 (2.73), 5.7931 (2.0), 5.566 (1.5), 5.738 (1.0) |
| $^{252}$Cf | 87.045% / 84.795% | 5.616-6.1183 | 6.1183 (84.0), 6.0757 (15.8), 5.9766 (0.2), 5.8263 (0.002) |

* Calculated from Cf decay
** Decays corrected from Oak Ridge National Lab measurements [50]

The procedure with the $^{241}$Am source placed pretreated and non-pretreated LiF discs in direct contact with the source and then placed the combination into a vacuum chamber. Vacuum was maintained at 4000 Pa. Exposure lengths varied from 3 to 33 hours. After exposure, samples were removed from the vacuum and separated from the source. The irradiated side of the LiF disc was placed in immersion oil and mounted on a glass coverslip where it was then inspected by CLSM.

A more robust method was required for the Cf source due to the hazards of handling an unsealed source. Thermally pretreated and non-pretreated LiF discs were used with a custom aluminum collimator. The collimator, depicted in

Figure 19 and shown in Figure 20, had two configurations that changed the distance from the source to the LiF detector face: 0.150 cm and 6.337 cm. These two configurations resulted in solid angles of 2.93 Sr (0.19%) and 6.36 Sr (36.98%) from the source, which was treated as a point source.

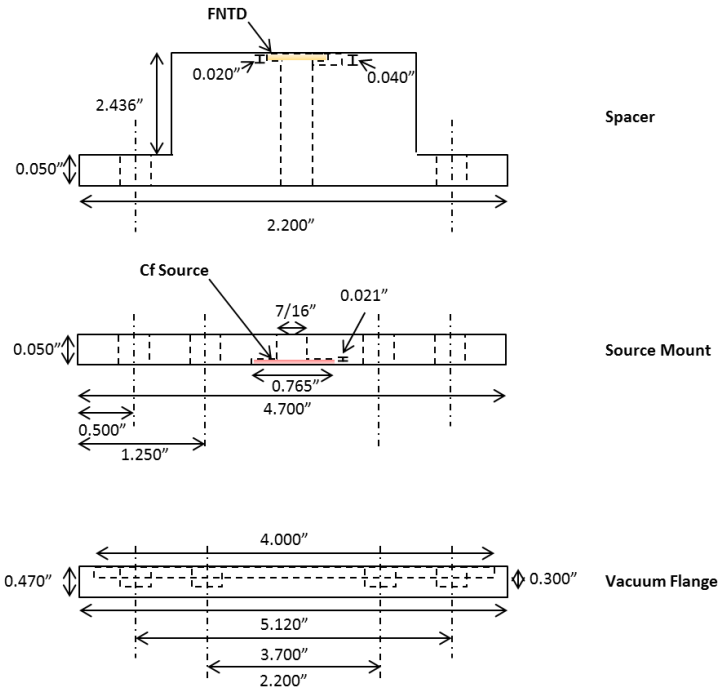



**Figure 19. A vertically exploded drawing of the right cylindrical collimator for Cf exposures. The FNTD is orange and placed on top of the spacer. The Cf source is red and placed in-between the source mount and vacuum flange. Ions traveled along the 7/16” diameter cylindrical column to impinge on the detector. Dimensions for the spacer shown are for the longer of the two configurations. Drawing is not to scale.**

The Cf source and FNTD were placed in the collimator and assembled into the vacuum chamber. The chamber was pumped to $1.05 \pm 0.01 \times 10^{-3}$ Pa and exposures varied between 2 mins to 72 hrs to control areal track density. The chamber was vented, and the samples were removed and placed in a gamma counter to obtain activity for verification of exposure to the Cf source and for shipping documentation to the University of Tennessee. At the University of

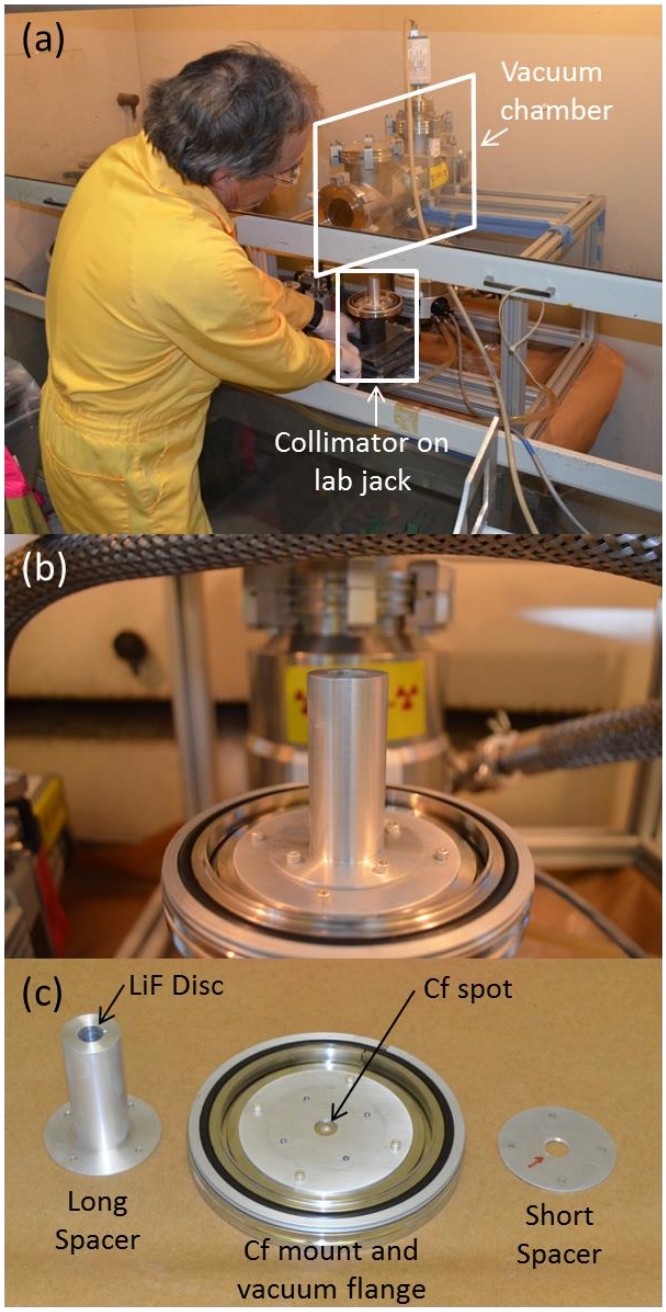



**Figure 20. Annotated pictures of the vacuum chamber and collimator prepared for assembly. (a) shows the assembled collimator ready to be raised and clamped into place. (b) close-up picture of the collimator ready to be raised and clamped into place. (c) dissembled collimator showing both spacers and the vacuum flange with Cf source mount. The Cf source and LiF disc are in their respective positions in all pictures expect for the short spacer in (c).**

Tennessee, examinations of the LiF with the CLSM used the same procedure listed above for the $^{241}$Am examinations.

All CLSM examinations of LiF samples used a 458 nm to simultaneously excite $F_2$ and $F_3^+$ defects in the irradiated surface. The laser used 14 mW dwelling for 35 ns to 3 µsec on each voxel. $F_4$-like defects were excited in a separate scan with 514 nm line from the argon laser with the same laser power and dwell time. The 63x/1.4 oil immersion objective inspected up to 35 µm into the irradiated surface with an airy disc of 1 (at 580 nm). Two HyD photomultiplier/ avalanche diode (PMT/AVD) detectors in count mode simultaneously collected the low intensity fluorescing light from 485-598 nm and 598-730 nm to obtain emission representative of $F_3^+$ and $F_2$ defects, respectively. When separately scanning for $F_4$-like defects, a single HyD in count mode collected low-intensity fluorescing light from 700-850 nm. With these parameters, a series of 2D images were collected and composited into a 3D image stack for analysis. Filters and other image alteration may be applied to obtain higher quality images for presentation in this work, but raw intensity and spatial data is always used in the quantitative analysis of images.

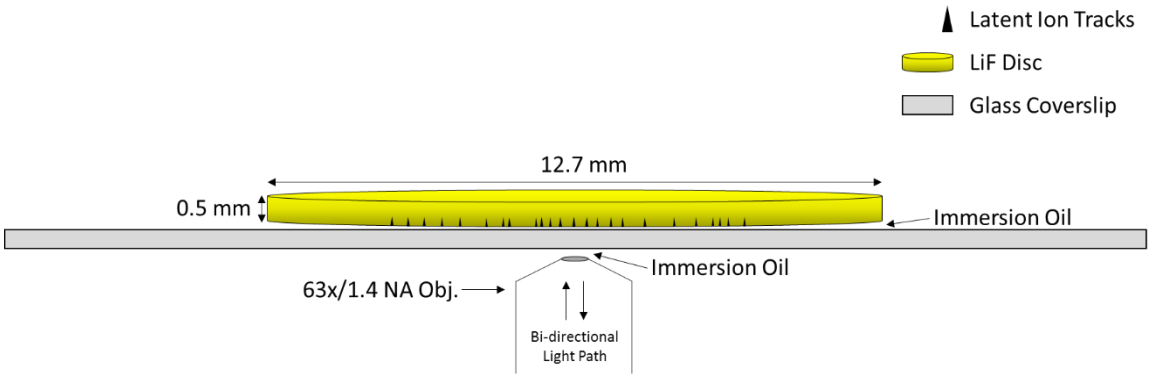



**Figure 21. Sample preparation for confocal inspection. Similar to Figure 18 excitation and collection occurs through the same objective lens with a glass coverslip holding the sample above the objective. Immersion oil is used as the coupling liquid between all solid mediums.**

Lecia image processing software was used to produce 3D images of tracks and initial analysis of aggregate image intensity data. Imagej was used to analyze track dimensions and intensities, apply filters and noise reduction, and process images with various track analysis programs [51].

## Results

Alpha tracks were suspected and later identified by exciting $F_2$ defects in crystals that did not receive thermal pretreatment. Initially, $F_2$ tracks could not be counted due to poor signal to noise ratio (SNR). Figure 22a shows areas of alpha damage with poor signal to noise. Faint horizontal lines can be seen in Figure 22a, each line is an alpha track. Figure 22b shows alpha tracks much more clearly in a thermal pretreated crystal. Pre-irradiation annealing of LiF crystals and improvements in fluorescing excitation and collection methods enabled counting of alpha tracks. Bilski's observations in December 2016 agreed with observations of alpha tracks and significantly improved confidence in alpha track identification [31].

Alpha decay occurs naturally along with spontaneous fission from three of the four the isotopes in the Cf source. Alpha tracks from the Cf source were compared to fission ion tracks (discussed in Chapter IV) for the expected ratio of 97 to 3. Empirical results found to average 100 alpha tracks to 4.2 ± 1.7 fission tracks after observing approximately 1000 alpha tracks over 4 samples.

Track intensity was observed for each defect type for 300 alpha tracks from the Cf source. Observations use summed track intensities. The distribution of track intensities for $F_2$ and $F_3^+$ defects are presented in Figure 23. The most intense $F_2$ track observed was 6844 arb. units, and the least intense was 1554 arb. units. The most intense $F_3^+$ track observed was 4389 arb. units, and the least intense was 739 arb. units. The average $F_2$ alpha track fluorescence observed was 3690 ± 70 arb. units compared to 1260 ± 30 arb. units for background. The average $F_3^+$ alpha track fluorescence observed was 2260 ± 20 arb. units compared to 2430 ± 60 arb. units for background. $F_2$ alpha tracks

appear with a broad normal distribution with intensity well above the average background of 1250 arb. units, and $F_3^+$ tracks appear with a narrow normal distribution. However, a major of this signal is equal to background intensity, 2425 arb. units.

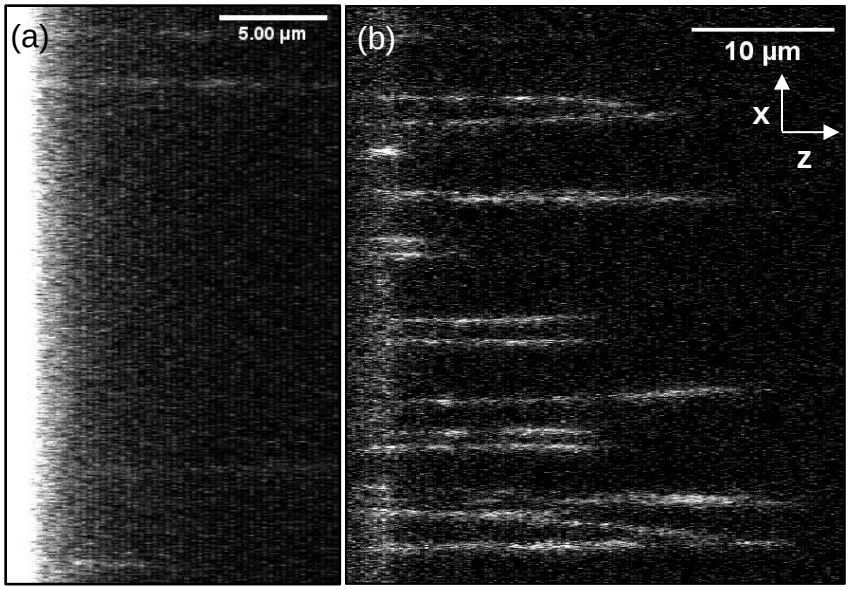



**Figure 22. $F_2$ fluorescence from alpha damage in LiF from Cf. The surface of the crystal is on the left side of the images along the x-axis and the alpha tracks are traveling from the surface into the crystal along the positive z-axis. (a) shows non-thermally pretreated LiF with a poor SNR. (b) shows thermally pretreated LiF with a significantly improved SNR from 4-M-60-L. In thermally pretreated LiF, alphas are counted and found to agree with expected ratios with fission tracks. Comparatively, the surface brightness in (a) is 28 times more intense than in (b), while the alpha brightness does not change appreciably.**

## Analysis

Self-shielding significantly increases the complexity of ion energies from natural sources like $^{241}$Am and Cf. For this reason, tracks of all energies up to the full decay energy are expected. Energy up scatter is considered negligible for a radiation field with such a low intensity.

Using regions of interest (ROI) placed around alpha tracks in $F_2$ images, alpha track locations were measured in the $F_3^+$ images. Signal was close to background with background being higher than the alpha track signal suggesting more data should be taken to draw conclusions, but alpha damage does not result in $F_3^+$ defects. This matches qualitative observations where no alpha tracks could be visually identified in $F_3^+$ images. $F_2$ signal averages above 3 times background and has a generally normal distribution of summed individual track intensities.

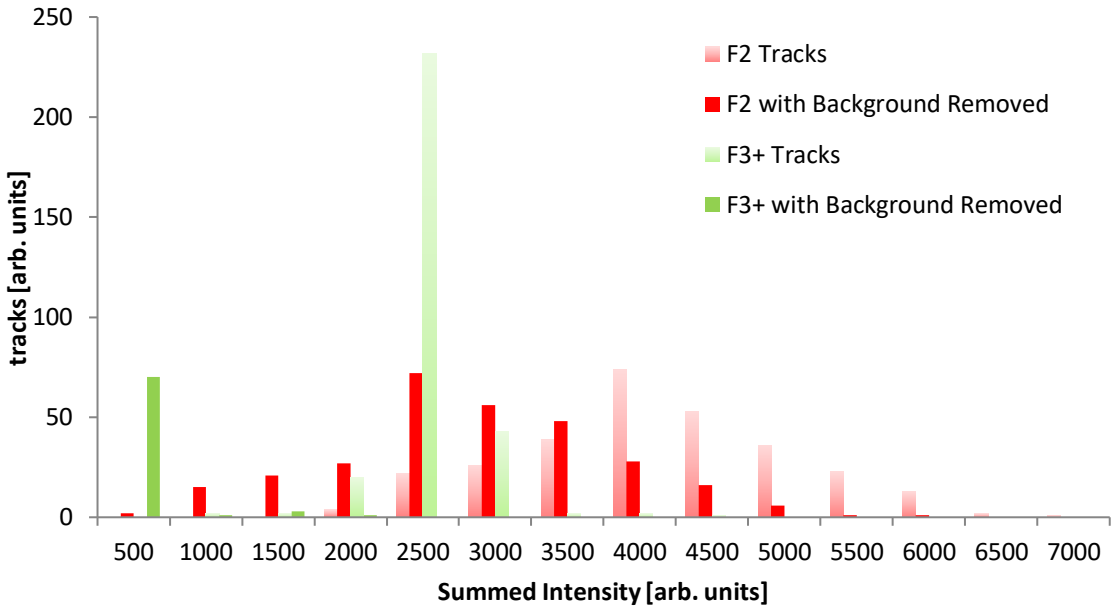



**Figure 23. Raw latent alpha track intensity distribution from Cf decay alpha tracks and intensities after background subtraction. Intensity is the total summed intensity of the ROI placed around the track.**

The lack of $F_3^+$ signal from alpha tracks is most likely due to the higher energy requirements for producing $F_3^+$ defects. F3+ production is more closely tied to the 10 keV $nm^{-1}$ threshold which alphas do not approach. Conversely in $F_2$ defects, the signal is dynamic across approximately the entire travel distance of the ion in LiF.

$F_2$ signal was relatively weak with a wide distribution. This weak signal was expected as alphas occur with <1 keV $nm^{-1}$ LET and lead to difficulties in their discovery and subsequent characterization. Their general shape is cylindrical with the radius and intensity behaving discontinuously relative to depth. This is partly explained by the increasing and decreasing behavior of the LET profile from SRIM models. As a result of this change, a gradual increase in intensity is expected over the first three quarters of the track, as seen by some of the tracks in Figure 22b. This behavior was exhibited by most tracks that exceeded 20 μm and by all tracks that exceeded 25 μm.

Tracks with length greater than 25 μm were observed but not predicted by SRIM models. This may be explained by the coincidental tracks or other radiations effectively reducing the density of the LiF within a 10 nm radius of the alpha's travel path [34]. Further research with mono-energetic alpha particles is recommended to fully explain this observation.

This analysis shows strong agreement between expected and observed gross alpha counts. The Cf track comparison is one of the principle verifications used that assess if identification of tracks is accurate. Differentiation of tracks occasionally overlap in summed intensity, but the two peaks of track intensities for fission and alpha are distinguished. Therefore, an intensity threshold of <7000 was used to identify alphas in $F_2$ signal, and an intensity threshold of <5000 was used to identify alphas in $F_3^+$ signal. This agreement at the described thresholds suggests that alphas and fission tracks are being accurately observed.

## Conclusion

The current detection is limited, and spectral analysis is inconclusive at this time. Comparing LiF to other fluorescing alphas track detectors like $Al_2O_3$:C,Mg, undoped LiF is a poor detector. Latent alpha track damage in LiF of $F_2$ defects can be discontinuous and fluoresces weakly. However, for this work, alpha tracks are useful in establishing an initial lower detection limit of fluorescence based on alpha's LET, i.e. <0.4 keV/nm from directly ionizing

radiation. It is seen in Chapter IV, when investigating induced fission events from fissile materials like uranium, natural alpha abundance is low and alpha's contribution to directly ionizing radiation dose is negligible.

The recent discovery of single alpha tracks in LiF makes continued effort in this area of work useful. Investigation of energy deposition behavior and mechanisms for energy transfer will strengthen understanding of ion interaction in solids at relatively moderate energies. This work is specifically promising for radiological medicine, space shielding (specifically inner layer, low-Z shielding), and ionizing radiation effects on electronics, as many components are surrounded by insulators with conduct band heights comparable to LiF.

# CHAPTER IV: CALIFORNIUM FISSION TRACKS

A number of important developments occurred during the investigation of californium fission product tracks in LiF. These include the initial discovery and confirmation of latent fission tracks, detector-specific sensitivity of fluorescence intensity to LET, LET dependent creation of different Frenkel defects, improvements in detector preparation, and improvements in fluorescing CLSM techniques. Ensuing comparisons to tracks in $Al_2O_3$:C,Mg led to confirmation that LiF is preferred over $Al_2O_3$:C,Mg for fission product identification. These advances enable fission characterization discussed in Chapters V and VI.

The Cf exposures described in Chapter III for alpha tracks were also used for fission track investigation. The experimental methods described in Chapter III are regularly referenced to in this Chapter. Notably all Cf exposures were principally designed to investigate latent fission tracks. Experiments were optimized to produce the broadest range of fluences possible below the detector saturation limit.

## Experimental Method

All LiF samples were irradiated and examined as described in experimental methods of Chapter III for the Cf exposures. However, $Al_2O_3$:C,Mg, or doped sapphire was also exposed and examined for fission tracks. Due to differences in the crystals shape and fluorescing defect properties, some minor adjustments were made to the experimental method.

The doped sapphires were 8 x 4 x 0.55 mm rectangular prism, single crystals provided for research by Dr. Mark Akselrod from Landauer, Inc. The $Al_2O_3$:C,Mg chips were polished below 1 μm on the prepared detector face. The fluorescing defects were second-order, electron-filled Frenkel defects from the anion sub lattice that are electro-negatively enhanced by the Mg dopant, written as $F_2^+$(2Mg) [30]. The $F_2^+$(2Mg) defects are excited with a 639 nm laser producing a fluorescence peak at 750 nm. The defects have excited state decay

time of 75 ± 5 ns [28]. The fluorescing properties of $Al_2O_3$:C,Mg resulting from swift heavy ion damage is well documented [30], [52].

A small bracket positioned a doped sapphire at the same location as the LiF discs in the collimator in Figure 19 and Figure 20. The bracket also added a 2° angle from the source to the detector face. The $F_2^+$(2Mg) defects were excited by the WLL with a 639 nm line inducing fluorescence that was collected by the HyD from 715 to 775 nm. As with LiF exposures using Cf, exposures were completed at the LTC, BWX Technologies Inc., and examination was completed at the University of Tennessee.

Fourteen exposures created twelve LiF samples and two $Al_2O_3$:C,Mg samples with various experimental parameters that are listed in Table 6. The range of exposure times and distances were designed to produce samples at regular areal track density intervals between the predicted saturation level and the minimum exposure time possible with this experimental setup. The predicted saturation limit was derived from Trautmann's description of track structure [53].

Table 6 lists the samples created with this method. Within the index numbers' 4 or 5 segments, important experiments parameters are labeled. The first number refers to the experimental series, approximately one year elapsed between series 2 and 4. Due to decay, the Cf source reduced 21% between series 2 and 4. The second segment is a letter denoting the length of the collimator, either S for small or M for medium. The third segment is the planned exposure time in minutes. The fourth segment indicates the detector type: L for LiF and A for $Al_2O_3$:C,Mg. The fifth segment is used for duplicates when the all of the previous segments are identical and an additional annotation is necessary.

To verify that observations of fluorescence from $F_2$ and $F_3^+$ and after examination of saturated tracks in 2-S-180-L, the disc was thermally annealed to remove defects. The disc was heated to 450 °C for 20 mins. The annealed LiF was found to have a homogenous distribution of low intensity fluorescence. The

**Table 6. Naming and experiemental parameters for Cf exposures of LiF and $Al_2O_3$:C,Mg.**

| Index Number | Exposure Time [min] | Distance from Source [cm] | Solid Angle [Sr] | Average Fission Track Fluence [particle $\mu m^{-2}$] | Average Distance between Tracks [µm] |
|---|---|---|---|---|---|
| 2-S-4320-L | 4318 | 0.254 | 4.647 | * | * |
| 2-S-1440-L | 1440 | 0.254 | 4.647 | * | * |
| 2-S-180-L | 300 | 0.254 | 4.647 | * | * |
| 2-S-20-L | 19 | 0.254 | 4.647 | $3.33 \times 10^{-1} \pm 1.7 \times 10^{-2}$ | 1.7 |
| 2-M-4320-L | 4320 | 2.7089 | 0.024 | $3.60 \times 10^{-1} \pm 5 \times 10^{-3}$ | 1.7 |
| 2-M-1440-L | 1440 | 2.7089 | 0.024 | $1.0901 \times 10^{-1} \pm 1 \times 10^{-5}$ | 3.0 |
| 2-M-180-L | 299 | 2.7089 | 0.024 | $2.08 \times 10^{-2} \pm 2.2 \times 10^{-3}$ | 6.9 |
| 2-M-20-L | 2.67 | 2.7089 | 0.024 | $4.17 \times 10^{-4} \pm 2 \times 10^{-2}$ | 49.0 |
| 4-M-1020-L | 967 | 2.7089 | 0.024 | $8.70 \times 10^{-2} \pm 2.86 \times 10^{-3}$ | 3.4 |
| 4-M-60-L | 61 | 2.7089 | 0.024 | $6.84 \times 10^{-3} \pm 1.01 \times 10^{-2}$ | 12.1 |
| 4-M-235-L-A | 241 | 2.7089 | 0.024 | $3.23 \times 10^{-2} \pm 4.69 \times 10^{-3}$ | 5.6 |
| 4-M-1020-A | 1020 | 2.7089 | 0.024 | ** | ** |
| 4-M-235-L-B | 235 | 2.7089 | 0.024 | $3.54 \times 10^{-2} \pm 4.49 \times 10^{-3}$ | 5.3 |
| 4-M-235-A | 235 | 2.7089 | 0.024 | ** | ** |

*Detector saturation occurred, track counting unreliable.
**Alpha particle tracks could not reliably be differentiated from fission tracks.

average intensity was 1.15 ± 0.03 x $10^{-6}$ arb. $\mu m^{-3}$ for $F_2$ emission and 2.07 ± 0.02 x $10^{-8}$ arb. $\mu m^{-3}$ for $F_3^+$, which agreed within 10% annealed non-irradiated blanks.

## Results

As reported above, the exposures listed in Table 6 occurred during two series of experimentation. The change in source activity was accounted for so that 180 minutes of exposure in series 2 was the same as 235 minutes in series 4. The three most heavily irradiated samples exceeded the saturation limit of the detector and were subsequently not used in analysis. The remaining sample that used the smaller collimator had a large percentage of tracks that were not normal to the detector face. In samples using the longer collimator, tracks that were not normal to the detector face occurred at approximately 1 in 50 normal tracks. The non-normal tracks are counted in gross track counts but, unless explicitly stated, are not included in other quantification.

Fission tracks appear in quantities appropriate for their exposure and geometry. Direct comparison to the Cf source intensity (measured by gamma analysis) is not reliable since source self-shielding of heavy ions has a complex and significant impact on ion energies arriving at the detector. However, the appearance of tracks does agree with expected changes in fluence when exposure time and geometry are varied. In Figure 24, the fluences observed in LiF are compared to their expected rate of change. The slope of the line is the change in exposure time and distance, and the y-intercept is based on a fit to the observed number of tracks. Observed densities agree well with anticipated densities strongly supporting that tracks observed were caused by heavy ions emitted from the Cf source.

Tracks appear as spots when viewed two dimensionally in the xy-plane. In Figure 25 and Figure 26, the xy-plane presented is a slice taken 3.6 ± 0.5 μm into the detector face (in the z-direction). Figure 25 shows size and spot intensities in LiF that change inversely to the defect order. The average

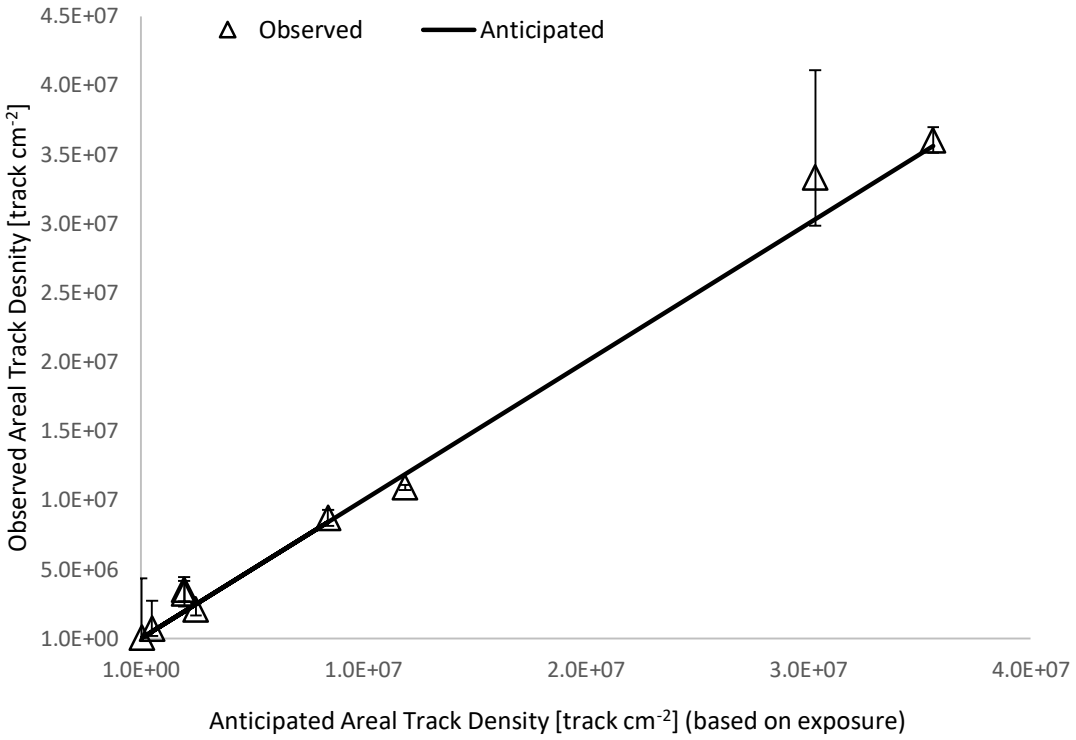



**Figure 24. A plot of the LiF samples listed in Table 6 comparing anticipated areal density to observed areal density. Anticipated values fall on the bold diagonal line. Standard error and a vacuum pumping uncertainty are applied to observed densities. The lowest fluence has an observed density of 4.17 x $10^4$ track $cm^{-2}$. The 3 x $10^7$ track $cm^{-2}$ anticipated areal track density data point was exposed with the smaller spacer; its error includes a larger exposure time uncertainty.**

fluorescent intensity for a spot in Figure 25 (a), (b), and (c) is 17920 ± 360, 12410 ± 780, and 5050 ± 170 arb. units, respectively. In Figure 26(a), spots in $Al_2O_3$:C,Mg are numerous due to higher sensitivity at lower LETs, specifically alpha particles [28]. A smaller field of view and lower fluence is presented in Figure 26(b) for better comparison to Figure 25. In Figure 26, clear delineation of fission tracks and alpha tracks is not evident.

Fission tracks when viewed in cross-section and three dimensionally are conical structures. Figure 27 shows a cross-section of a representative fission track alongside an alpha track in a non-pretreated LiF detector. Without pretreatment, the surface appears as an intensely fluorescing region at the bottom of the figure. The fission track is much shorter than the alpha track and is shorter in $F_3^+$ compared to $F_2$ agreeing with the expected relationship fluorescing intensity is inverse to defect order. The fission track length from $F_3^+$ in Figure 27a is 5.7 μm and from $F_2$ in Figure 27b is 6.6 μm. As reported in Chapter III, the alpha track is not present in the $F_3^+$ image and is 14.4 μm long in the $F_2$. The average voxel intensity of the fission track, when excluding the surface region, is 4.1 for $F_2$ and 3.2 for $F_3^+$.

Forty-three tracks were observed for each type of defect. Observations reported were taken from thermally pretreated detectors, those beginning with 4-M. The distribution of track intensities is presented in Figure 28. The values are the sum of total intensity without background subtraction. The most intense $F_2$ track observed was 116654, and the least intense was 11347. The most intense $F_3^+$ track observed was 57237, and the least intense was 5533. The most intense $F_4$-like track observed was 87312 and the least intense was 20645. The $F_4$-like intensity disagrees with the inverse intensity to defect order rule when the entire track is summed. If the $F_4$-like spot is measured individually in each slice, then we see that $F_4$-like tracks are longer with more intense track cores. Unlike alphas, fission tracks intensities do not present with a normal distribution; however, the minimum desired bin height of 10 is not achieved with the on-hand data preventing reliable description of behavior.

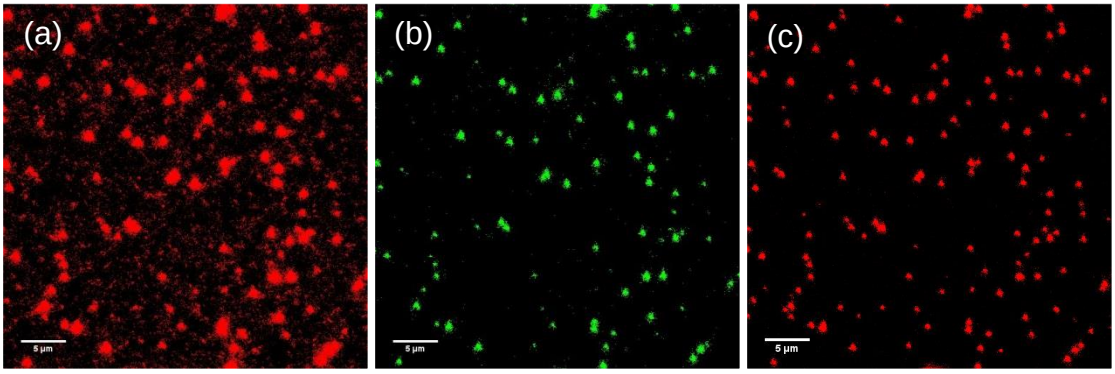



**Figure 25. images of LiF, sample 4-M-1020-L, taken 3.6 ± 0.5 µm into the surface of the detector. (a) is collection of $F_2$ signal. (b) is collection of $F_3^+$ signal. (c) is collection of $F_4$-like signal. Each spot is a fission track. Alpha tracks are not easily observable in (a) due to contrast and brightness settings. Scale bars denote 5 µm.**

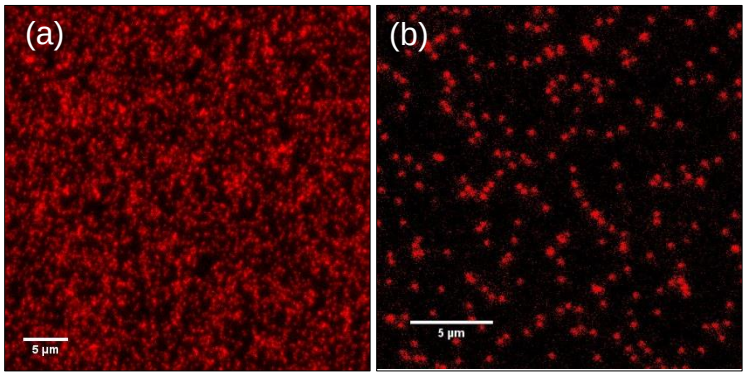



**Figure 26. images of $Al_2O_3$:C,Mg taken 3.6 ± 0.5 µm into the surface of the detector. Each spot is either an alpha track or fission track. Due to high signal from alpha tracks and relatively low signal difference between alphas and fission tracks, a lower intensity exposure is shown in (b). (a) is collected from 4-M-1020-A. (b) is collected 4-M-235-A, approximately a 77% reduction in track density form (a). Scale bars denote 5 µm.**

## Analysis

For the samples listed in Table 6, those employing the smaller collimator had the least useful data. Poor beam collimation and high areal track density made quantitative analysis difficult since single tracks could not be isolated. During experimental design, Trautmann's work suggested a

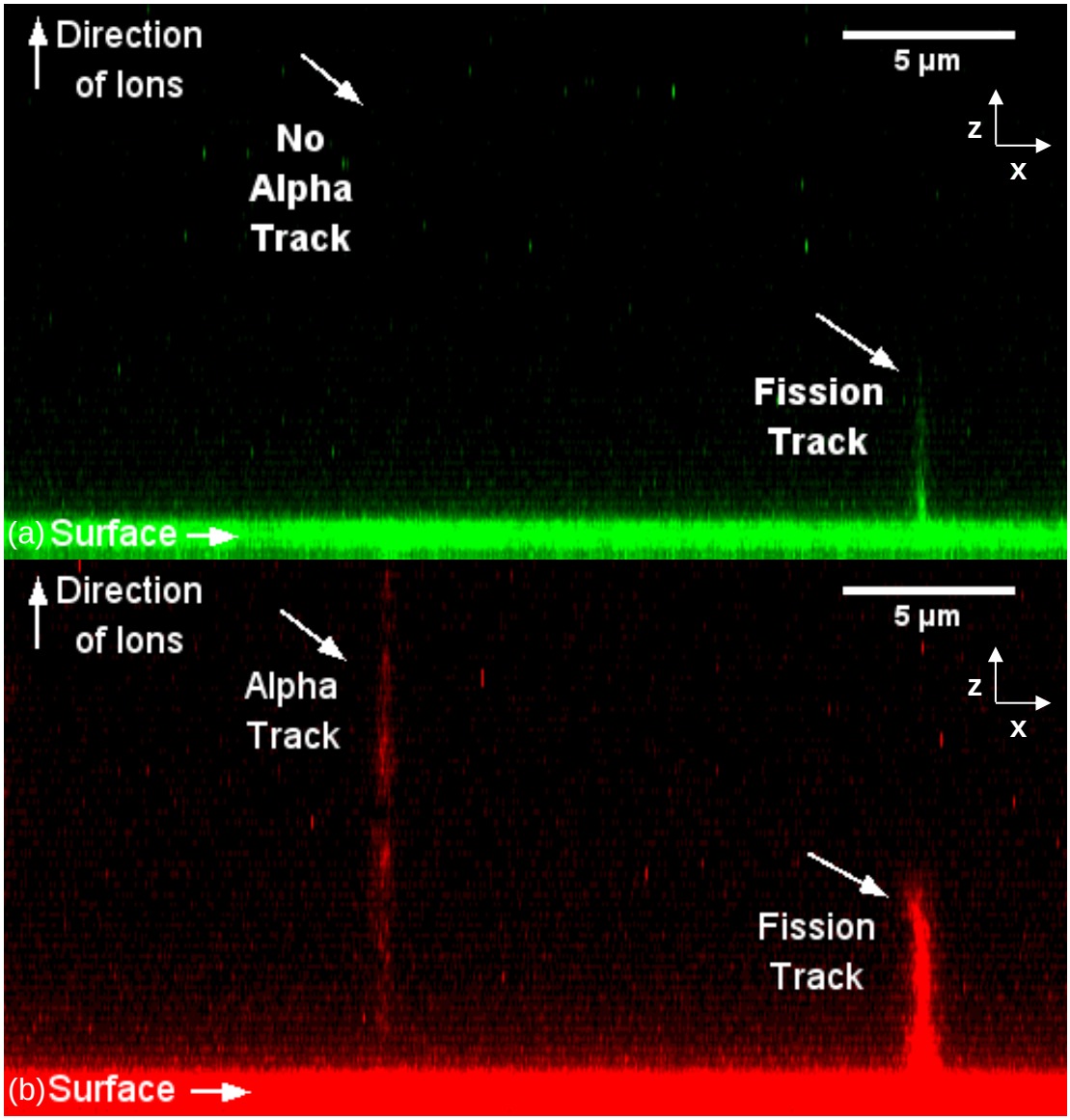



**Figure 27. Images are cross-sectional 30.8 µm x 10.5 µm x 16.1 µm projections from LiF sample 2-M-20-L. Images are the raw intensity data utilizing the maximum intensity voxel in projection to compress the y-axis into a single frame. (a) is a monochromatic image of $F_3^+$ emissions. (b) is a monochromatic image of $F_2$ emission. The irradiated surface is the bright edge along the bottom of the images. The incident ions are in the positive z direction. An alpha track is present on the left side of (b) but is not visible in (a).**

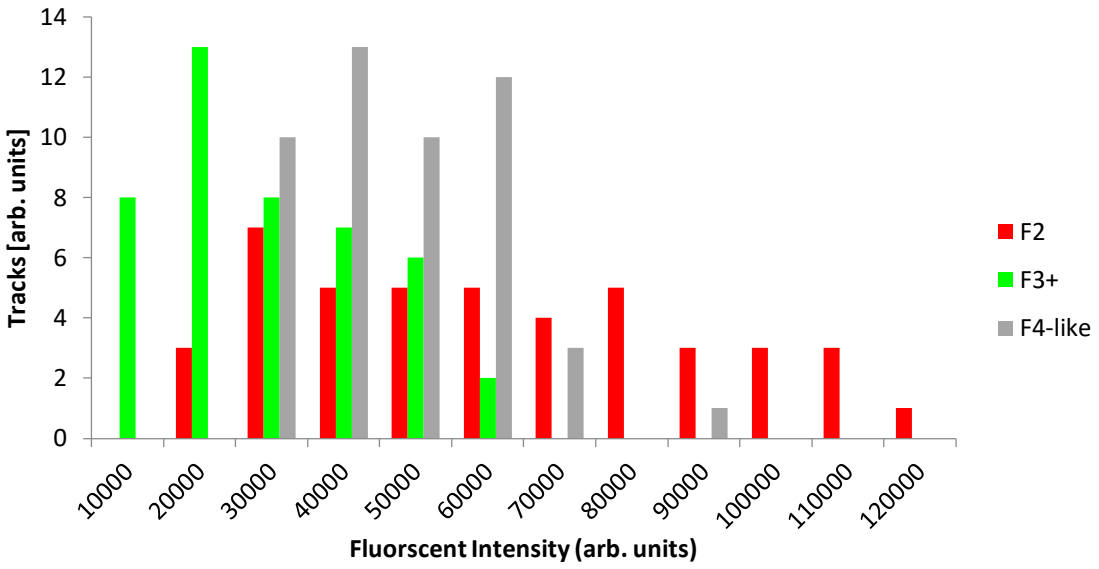



**Figure 28. Latent fission track intensity distribution from Cf SF from thermally pretreated samples. Intensity is the total summed intensity of the ROI placed around the track in each image. Intensities are raw intensity values observed within the ROIs.**

saturation of tracks at a fluence of $1x10^{9}$ to $1x10^{10}$ tracks $cm^{-2}$ [54]. This was based on thermal spike model prediction of 40-60 nm diameter F-centers regions. After observation, fission tracks presented with diameters up to 1.6 µm. As a result, the highest fission product fluences with the small spacer could not be effectively evaluated. In Bilski ‘s work, observed alpha tracks were similarly large compared to theoretical values, 500 nm diameters [31]. Alpha observations from this study agree with Bilski’s alpha track size results and continue the trend of large fluorescence areas around the track with much larger fission track diameters than those predicted by thermal spike models. Bilski’s work suggested that better resolution microscopy may correct this size issue. The spherical aberration and magnification improvements recommended by Bilski are largely absent through the use of a laser scanning system with an improved objective. This suggests that either these observations are the correct size or other factors are contributing to the size difference. In the coulombic explosion model, additional energy is added to the Bethe-Bloch energy transfer from the ion by a

potential energy to kinetic energy transition in the crystal. As described in Chapter II, this event will cause Li and F nuclei to repel one another adding to the damage around the track area.

The use of a laser scanning microscope introduces other considerations. One major consideration regarding the size of these tracks is Raleigh's diffraction limit, which restricts the microscope's resolutions. As discussed in Chapter II, the PSF, under optimal conditions, prevents resolution below 130 nm in the xy-plane. This can be presented as an uncertainty of features when evaluating at or below this size. As described in equations 6 and 7, the minimum voxel collection size is approximately 130 x 130 x 900 nm. The microscope uses galvanometric operated mirrors to make tens of picometer adjustments that enable presentation of voxels smaller than the diffraction limit. These sub-diffraction limit voxels are linearly deconvolved from the diffraction-limited collection voxels. This process is good for presenting larger objects like major features of animal or plant cells at tens of microns but smears fluorescence of lateral track features that occur at scales of hundreds of nanometers. As a result, any voxel presented by the microscope must have an associated xy-plane uncertainty of 130 nm and a linear weighting vector that focuses intensity towards more intense voxels. The interpretation of 1.6 μm tracks, therefore, is 1.6 ± 0.26 μm with a weighted distribution toward -0.26 μm.

Due to the complex nature of self-shielding, fission product fluence on the surface of the detector could not be estimated directly from the neutron or gamma activity of the source [55]. For this reason, internal agreement with changes in exposure is used in Figure 24. Standard error is combined with uncertainties produced from the experimental method. Agreement with the alpha-track to fission-track ratio presented in Chapter III and the internal agreement with exposure times presented in Figure 24 make it extremely likely that the observed latent tracks reported above are induced by fission daughter ions.

Upon initial inspection, all defects intensities from fission tracks decrease as a function of depth. This trend agrees with LET behavior in SRIM models,

presented in Figure 30. Additionally, this is different as compared to observation and modeling of alphas which may not have a continuously decreasing LET, and therefore, alpha track intensity increases or remain constant. However, when inspect single tracks, all three defect trend downward inconsistently, shown in Figure 29. SRIM and the CSDA predict a smooth curve. After observing similar depth-dependent irregularities in a red Chroma auto fluorescent slides, the inconsistencies are attributed to a systematic effect of the collection method. Working with the Lecia applications scientist, the inconsistencies may be explained by the low light fluorescence and the quantum efficiency of the detector.

The tracks shown in Figure 30 are from a thermally annealed sample. In samples without annealing, irregularities were more serve. Alpha tracks or other forms of radiation may contribute to the irregularities; however, none of these modes of damage are expected to generate the significant changes seen within the first 3 microns of the surface, and the impact is considered negligible.

Figure 30 shows the SRIM LET predictions for the most likely fission products and the heaviest and lightest products. Figure 31 shows the averaged intensity of fluorescence for 49 tracks for each defect type. Once averaged, the intensities smooth out and a reliable behavior is identified. Defect production is a function of energy deposition into the medium; however, the Bethe-Bloch model for collisional energy disposition is insufficient. As mentioned above, this is likely due to the coulombic explosion adding energy to the detector via state change in the vicinity of the ion strike. If this repulsion is found to be similar or greater than the local energy deposition by the impinging ion, then the differences between Figure 30 and Figure 31 may readily be explained. Additionally, the track radius and core radius shown in Figure 32 and discussed below should be related to this columbic model.

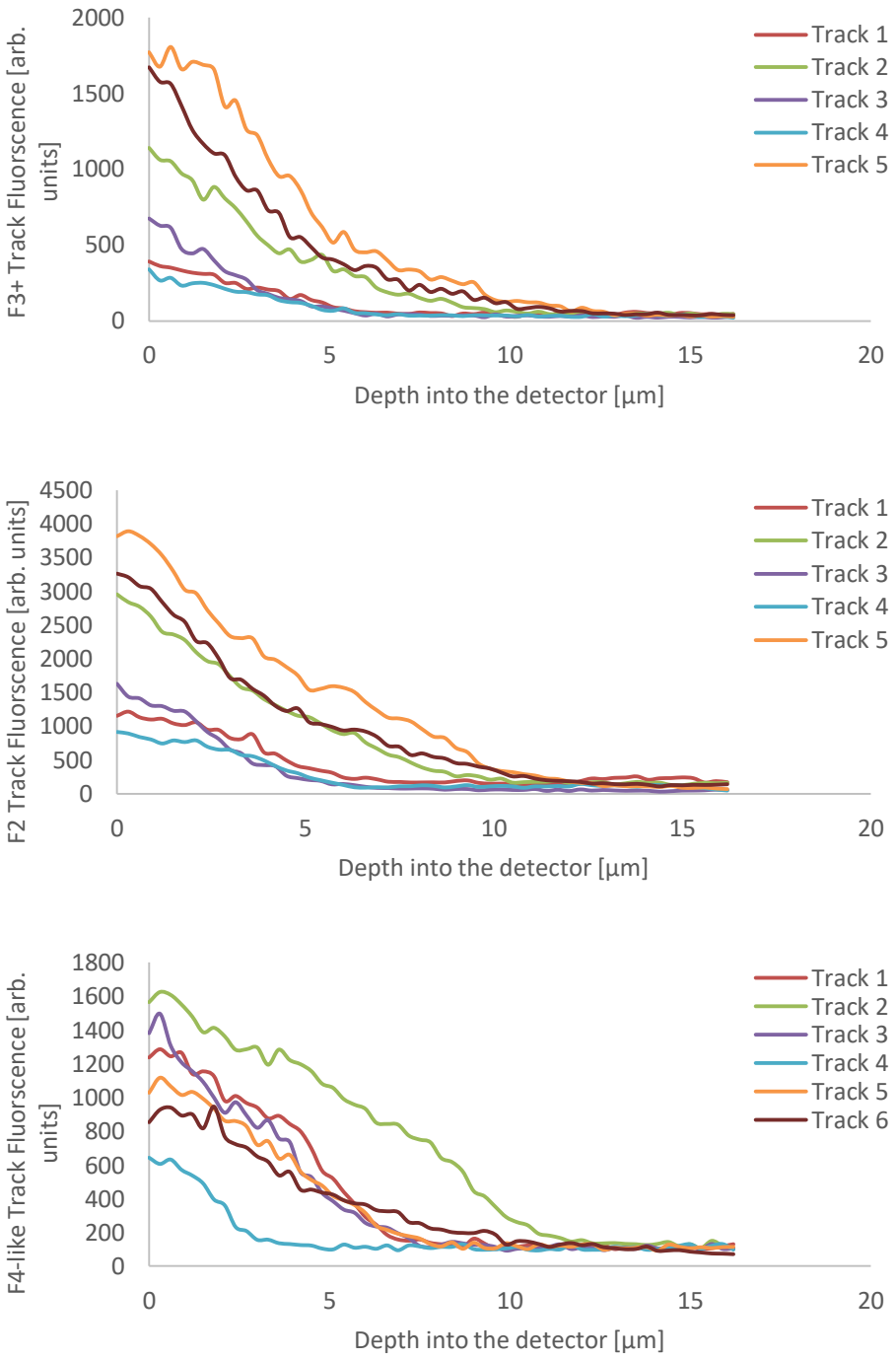



**Figure 29. Fluorescence intensity versus depth plots for six randomly selected tracks. The surface of the detector starts at depth zero. The graphs highlight the inconsistent decrease in intensity of single tracks.**

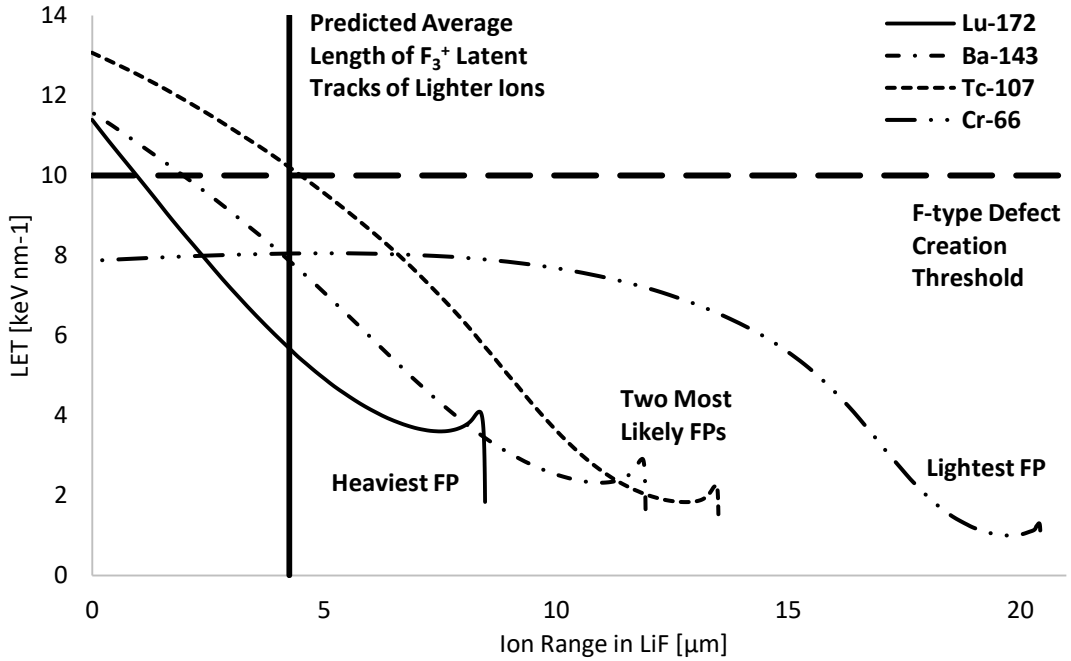



**Figure 30. SRIM modeling of LET for the pair of most abundant, the lightest, and the heaviest $^{252}$Cf fission products as a function of penetration depth in LiF [56]. The thick dashed horizontal line is the threshold above which F-defect creations likely by columbic explosive dislocation, whereas decay of self-trapped excitons is more likely below this threshold [34]. The dark vertical line represents the approximate depth at which the many ions are expected to produce significantly fewer fluorescing defects. This chart shows that while most tracks will have a roughly linear decreasing energy transfer to the crystal until the end of the track, at a point below 4.3 µm all tracks should have a nonlinear change in fluorescing intensity. Also, from models and indicated in this graph, no fission product is expected to penetrate deeper than 20.5 µm into the crystal and a significant majority will penetrate less than 16 µm.**

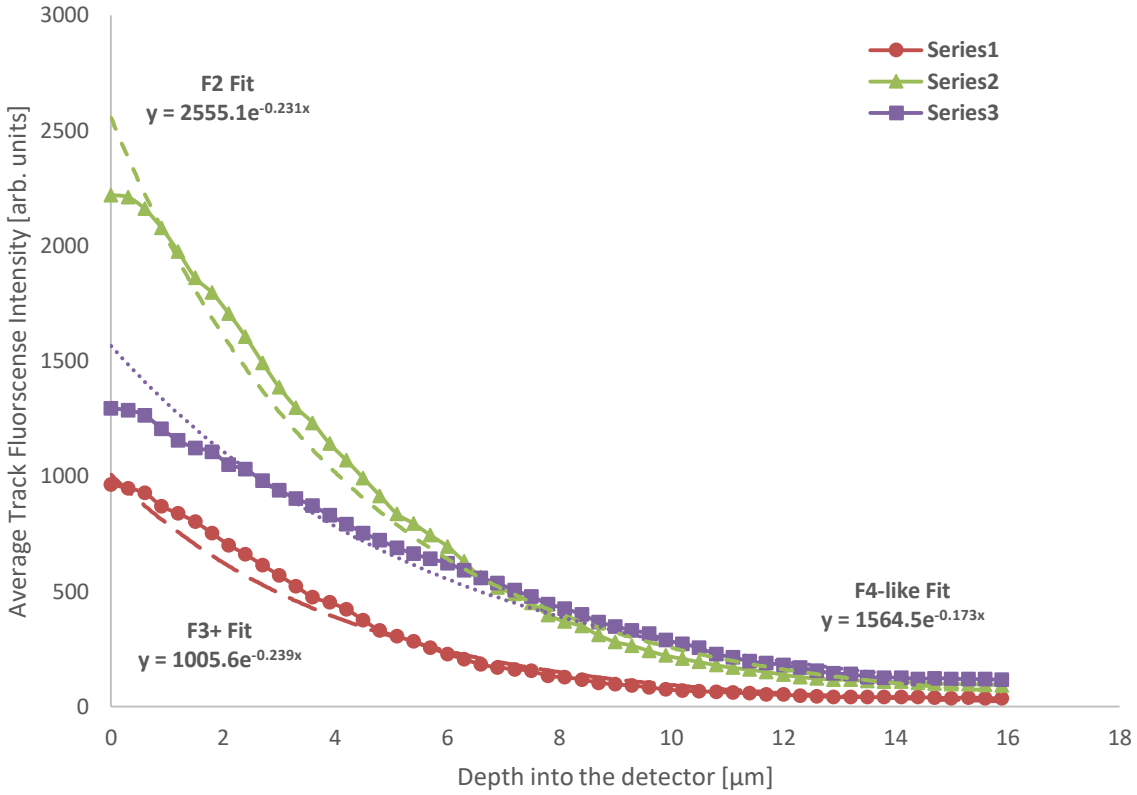



**Figure 31. Average fission track fluorescence of 49 tracks from 4-M-235-L-A. Crystal surface is at zero depth. Tracks observed are an average of all tracks within a 40 x 40 µm area. In general, the area was randomly selected from the center of the irradiated surface. Exponential trend lines are fitted to each data set showing a similar behavior across the defect types with $F_4$-like behaving almost linearly. Each fits' coefficient of determination, $R^2$, is above 97% reflecting a good fit. Data is raw intensity collected. No background correction or other subtracts were performed.**

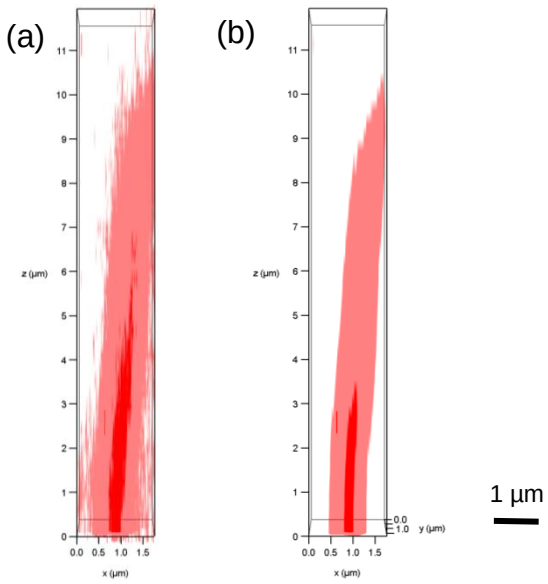



**Figure 32. $F_2$ emission from a latent fission track. (a) is raw fluorescence data showing incoherent signal around the edges of the inner and outer regions of the track. (b) is the same track using a median filter to reduce noise thereby presenting a smoother and, due to the low light environment, overall reduced intensity. Per voxel, white is 0-1 intensity, light red is 2-7 intensity, and dark red is 8-32 intensity.**

$F_2$ tracks exhibited a fluorescent core. These cores were generally 10 times more intense than the outer edges of the track. A representative cross-section of a track is presented in Figure 32. This core structure is most likely the result of coulombic explosive activity which is localized to the region were LiF is highly ionized. In later work, $F_4$-like tracks had a signal overlap with Li collide, which may form in the track center after F-F diatomic gas forms in the tracks during cooling, leaving Li collides.

Not shown in the data presented above are the fluorescing intensities outside the surface of the crystal. Each defect produces a different glow that occurs before the surface of the defect and most pronounced by the $F_2$ defects. Partially this is glow from the smearing effect mentioned at the beginning of this section and is more serve than the lateral smearing since the z direction suffers a 0.9 µm minimum voxel collection size. Additionally, hillock structures around the area of the strike are small but protrude from the surface adding to the glow [57].

# Conclusion

Latent tracks were identified in LiF. Track frequency and behavior agreed with multiple known relationships and compared well to tracks in other mediums strongly indicating that tracks were produced from fission daughter ions.

Tracks appeared larger than expected generally agreeing with the similar observations from alpha tracks. Some unexpected behaviors were identified as systematic effects from CLSM. More interestingly, most unexpected behaviors are explained by coulombic explosion, which magnifies previously anticipated damage from unattentuated fission products. Further work is needed to explore and verify this hypothesis.

This early work should undergo peer review and replication by other researchers. Excitingly, this work suggests a deeper understanding of directly ionizing radiation damage and may allow for ion spectral analysis in the future with a LiF FNTD. However, it is my opinion that pure LiF will not allow for the required sensitivity to achieve spectral analysis for isotopic identification of a source and other FTND should be investigated.

# CHAPTER V: URANIUM FISSION TRACKS

Uranium was exposed to a moderated neutron field from a $^{252}Cf$ source to induce fission. This experiment included a principle prototype test for the production of latent fluorescent signal in LiF from fissile material, specifically for use in enrichment analysis. The identification of tracks and subsequent counting of tracks was essential for identifying enrichment. This Chapter discusses the modeling, design, and experimentation with the irradiator and the subsequent track identified in LiF from the uranium. Chapter VI discusses enrichment calculations and predictions.

## Experimental Method

A custom irradiator was designed, modeled, and fabricated for a 1.215 Ci $^{252}Cf$ source (2.34 mg) to irradiate FNTD stacks containing various National Institute of Standards and Technology (NIST) uranium samples. Irradiations were completed at the Lynchburg Technology Center at BWX Technologies. CLSM analysis of LiF samples was completed at the UTK.

By priority, design of the irradiator considered cost, ready availability of moderating/shielding materials, simplicity, weight, and size. Models were completed for various designs in MCNP 6.0. Some modeled irradiator designs included a large solid high-density polyethylene (HDPE) cylinder; HDPE beads and steel; solid HDPE, steel, and hafnium; and a small amount of HDPE and mostly water. HDPE was heavily considered due to its relative low cost, low chemical reactivity, structural integrity, and its excellent neutron moderating qualities. A design using a HDPE core, surrounded by water contained in a 110-gal steel drum was selected for its ~$950 cost, <2.5 kgs. of principle components (the HDPE core) and ease of access to its principle shield and moderator, water. Figure 33 is a detailed drawing of the HDPE core where the source was placed in the central port and four smaller sample ports were array around the source. The core was housed at the center of the irradiator shown in Figure 34. The bottom HDPE plug and top HDPE plug were used primarily to position the core in the

center of the 110-gal drum. Plugs and the core were placed into a PVC pipe that prevented the source from moving to one side of the container and creating a high-radiation area outside of the irradiator.

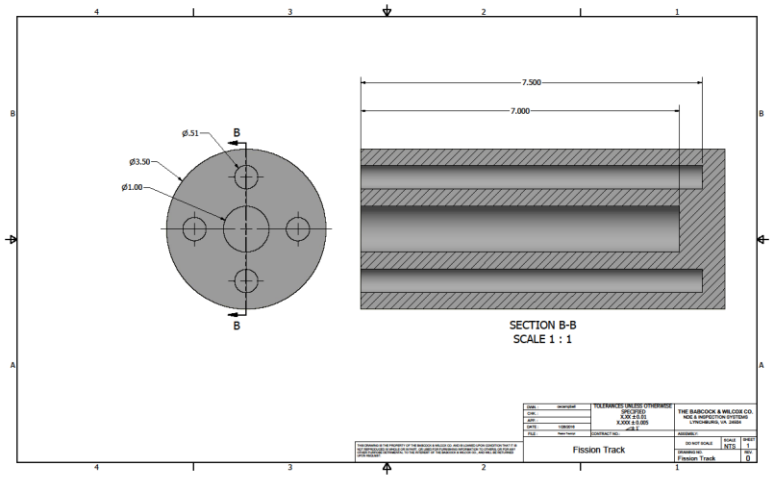



**Figure 33. Irradiator core drawing. The source port is the large center port. The sample ports are the four smaller ports arrayed around the center. Thin steel wire was wrapped and taped to the core for remote handling. Three threaded handling sockets allowed for removal from the irradiator incase the primary means of removal was not functioning properly.**

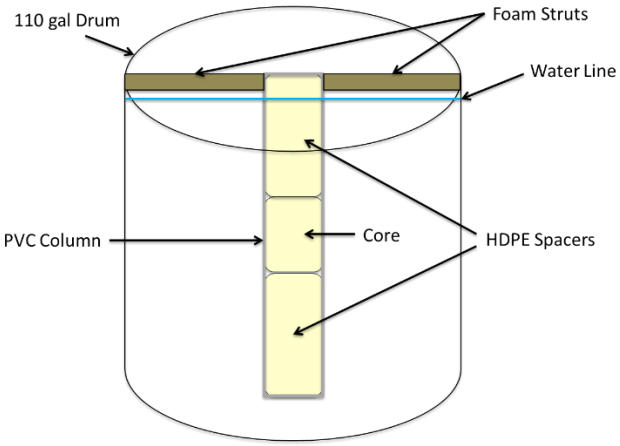



**Figure 34. A diagram of the 110-gallon steel drum irradiator. The drum was filled with water to moderate the neutron field.**

MCNP models were used to analyze the neutronics of the irradiator in order to achieve the highest thermalization possible with the design considerations listed above. The final model's geometry and thermal flux density are depicted in Figure 35. The models showed that with an all water design outside the HDPE core a 12% thermalization could be achieved inside the sample ports. Other configurations using various HDPE and water configurations varied approximately 3% from this thermalization value. With the sample ports evenly distributed radially about the source, the highest effective flux occurred in the third sample position up from the bottom. Three group neutron energy modeling was used to assess the quality of the neutron field. The thermal flux was evaluated as neutrons < 0.025 eV, epithermal from 0.025 eV to 4 eV, and fast from 4 eV to 14 MeV. Modeling showed that a better capture value in uranium could be achieved by placing samples very close to the source special form container, preferable in contact. Therefore, a special polyethylene spacer was made to hold a sample and placed below the source in the source tube. Modeling not only improved and guided the design of the irradiated but supplied the necessary information to predict fission behavior in the fuel particles. To validate the model, Ni, Fe, Co, and Cu dosimetry foils and wires were placed in and around the core.

Samples used National Institute of Standards and Technology (NIST) standard $U_3O_8$ listed in Table 7, inert chromium, thorium ($^{232}Th$) oxide, and cellulose nitrate without fuel as a blank. Three samples contained a mix of the listed materials. All other samples were single-material samples. Additionally, polyethylene plastic discs of the same size as the LiF discs were obtained from Track Analysis Systems Ltd. (TASL) for traditional chemical etching comparison and replaced LiF discs in eight of the samples.

FNTDs were assembled with various fuel enrichments list in Table 7. SEM analysis identified $U_3O_8$ fuel particles to have a size range <0.1 µm to approximately 150 µm. U200 particles, described in Table 7, are seen in Figure 36. Noticeably, particles larger than 0.5 µm are comprised of many smaller

particles. Droplet dispersion was used to control fuel distribution on the LiF discs. Dispersion was verified with optical microscopy. Fuel particles were glued to the FNTD with a solution of cellulose nitrate and ethanol based on a Finnish methodology [58]. Figure 37 shows a diagram of the assembled FNTDs. Particles were placed in a solution of 150 mL ethanol and 25 mL cellulose nitrate. Cellulose nitrate concentrate was reduced to the lowest level possible while still holding the particle to the detector. This lower limited concentration was selected to reduce the amount of attenuating material between the particles and the detector face.

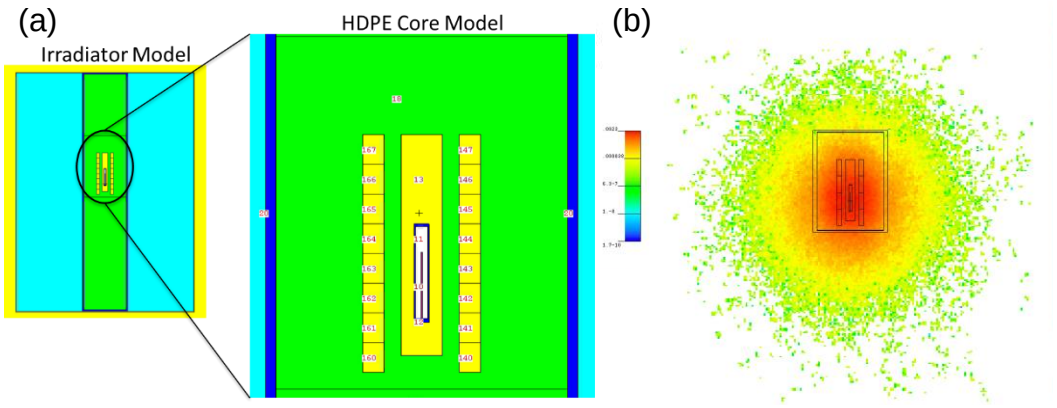



**Figure 35. MCNP model geometry (a) and thermal neutron flux (b) for the irradiator. A thermalization of roughly 12% was achieved in the sample ports from a $^{252}$Cf sources. (b) shows only the core model with the neutron field slightly heterogeneous about the source. The source was modeled as a line source to best approximate the platinum wires containing the $^{252}$Cf. The flux fraction heat scale in (b) reads from top to bottom 2.9 x $10^{-3}$, 3.8 x $10^{-5}$, 6.8 x $10^{-7}$, 1 x $10^{-8}$, and 1.7 x $10^{-10}$.**

Experimental execution required deliberate planning and effort on the part of many technical personnel at the LTC. The source presented a hazard when handling since it radiated a field of 2.5 rem $hr^{-1}$ at 1 meter from the source when in air. Rehearsed preparation enabled technicians to maintain a dose that was as low as reasonably achievable while the source was in air. Following extraction of

**Table 7. NIST $U_3O_8$ standards used in experiments and their respective isotopic atomic percent.**

| Name | % $^{234}U$ | % $^{235}U$ | % $^{236}U$ | % $^{238}U$ |
|---|---|---|---|---|
| U005 | 0.00218 ± 0.00004 | 0.4895 ± 0.0005 | 0.00466 ± 0.00005 | 99.504 ± 0.001 |
| U010 | 0.00541 ± 0.00005 | 1.0037 ± 0.0015 | 0.00681 ± 0.00007 | 98.984 ± 0.001 |
| U020 | 0.0125 ± 0.0001 | 2.038 ± 0.002 | 0.0165 ± 0.0001 | 97.933 ± 0.002 |
| U030 | 0.0190 ± 0.0001 | 3.046 ± 0.003 | 0.0204 ± 0.0001 | 96.915 ± 0.003 |
| U050 | 0.0279 ± 0.0001 | 5.010 ± 0.005 | 0.0480 ± 0.0002 | 94.915 ± 0.005 |
| U100 | 0.0676 ± 0.0002 | 10.190 ± 0.010 | 0.0379 ± 0.0001 | 89.704 ± 0.010 |
| U150 | 0.0993 ± 0.0002 | 15.307 ± 0.015 | 0.0660 ± 0.0002 | 84.528 ± 0.015 |
| U200 | 0.1246 ± 0.0003 | 20.013 ± 0.020 | 0.2116 ± 0.0006 | 79.651 ± 0.021 |
| U350 | 0.2498 ± 0.0006 | 35.190 ± 0.035 | 0.1673 ± 0.0005 | 64.898 ± 0.036 |
| U500 | 0.5181 ± 0.0008 | 49.696 ± 0.050 | 0.0755 ± 0.0003 | 49.711 ± 0.050 |
| U750 | 0.5923 ± 0.0009 | 75.357 ± 0.025 | 0.2499 ± 0.0008 | 23.801 ± 0.024 |
| U850 | 0.6437 ± 0.0014 | 85.137 ± 0.017 | 0.3704 ± 0.0011 | 13.848 ± 0.014 |
| U930 | 1.0812 ± 0.0020 | 93.336 ± 0.010 | 0.2027 ± 0.0006 | 5.380 ± 0.005 |

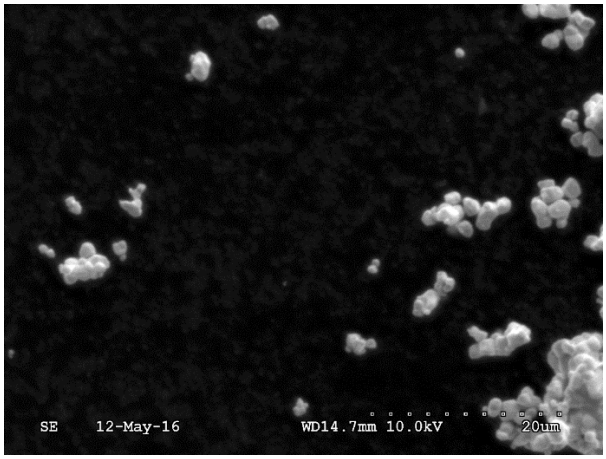



**Figure 36. SEM image of U200 on carbon tape to verify size of particles. Most particles are clearly a collection of smaller, submicron particles.**

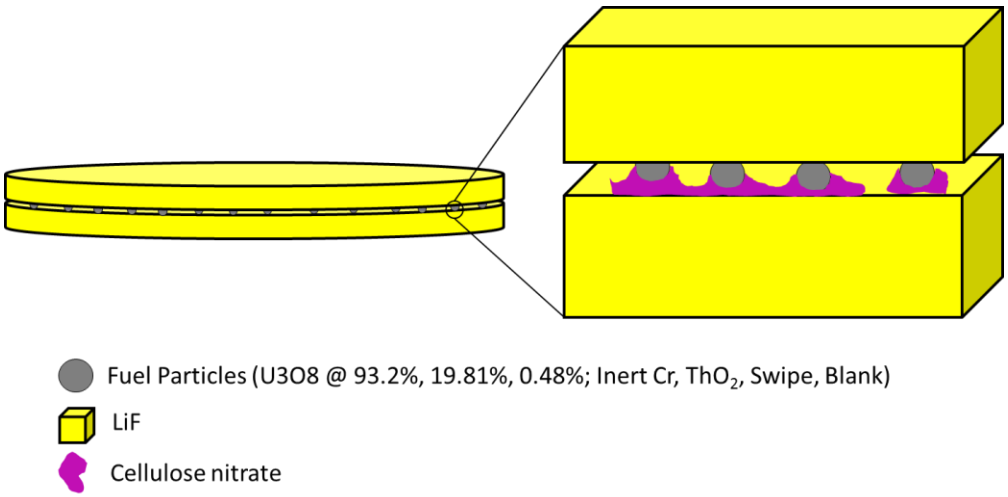



**Figure 37. Detector and fuel diagram shows a detector 'sandwich' around the fuel particles. Particles are adhered to the crystals with cellulose nitrate to maintain registration of particles.**

the core, samples were taken to the counting lab for fission product analysis with gamma spectroscopy. Identified fission products agreed with irradiated fuel libraries and radiation intensities were below exempt quantity amount, as determined by the Department of Transportation threshold, for transportation to UTK. This low radiation level is an important qualitative measure of the high-sensitivity at low-intensity levels after activation.

In total, the 83 FNTD pairs shown in Figure 37 were created from three different exposures. After geometry, enrichment, and time consideration, a possible range of fissions in a 10 µm particle was expected between 0 and approximately 832. In a 1 µm particle, this range was reduced to 0 to approximately 275 fissions. This range was designed as to provide the greatest opportunity to develop a large number of data points for mapping enrichment while also providing repeatability.

Dosimetry was included with samples and in designated locations to validate computer modeling. Co, Cu, Ni, and Fe dosimetry foils and wires were used to validate the model's thermal and fast flux predictions. These neutron dosimeters were counted with gamma spectroscopy after the final exposure.

The intended inspection method with the CLSM differed from samples created by direct $^{252}$Cf exposures discussed in Chapter IV. These samples were face-down on the coverslip, which made inspection by short-working distance objectives possible, specifically the 63x. However, keeping the FNTD sandwich together so that $4\pi$ detection could be achieved was preferred for these experiments. To accomplish this, the CLSM had to image through the LiF disc, nominally 500 ± 100 µm of LiF. Initially, an image with the 40x oil was taken using standard two µm fluorescence beads, Figure 38; however, this could not be repeated in samples with weaker signal. Additionally, the 669 µm is significantly greater than the 240 µm working distance of the 40x oil objective. This result suggests that Figure 38b is a holographic reflection of the top surface of the LiF, and the position reading on the stage is the result of the objective lifting the coverslip. After testing, using a water surrogate, optical gel, with the 40 times water objective was selected to view through the LiF disc. The 40 times water immersion objective has a working distance of 650 µm,

This method of imaging through the LiF detector was resolved, however, image quality was significantly reduced. To obtain quality images for quantitative analysis and for presentation in this work, the original method presented in

Chapter IV was used. Again, this method places the irradiated side, in this case containing fuel, in immersion oil and positioning the disc face-down on the coverslip so that the 63 times oil immersion objective could image the sample. This method retains shadows cast by large particles and reduces the $2\pi$ geometry of the detector minus the shadowed area.

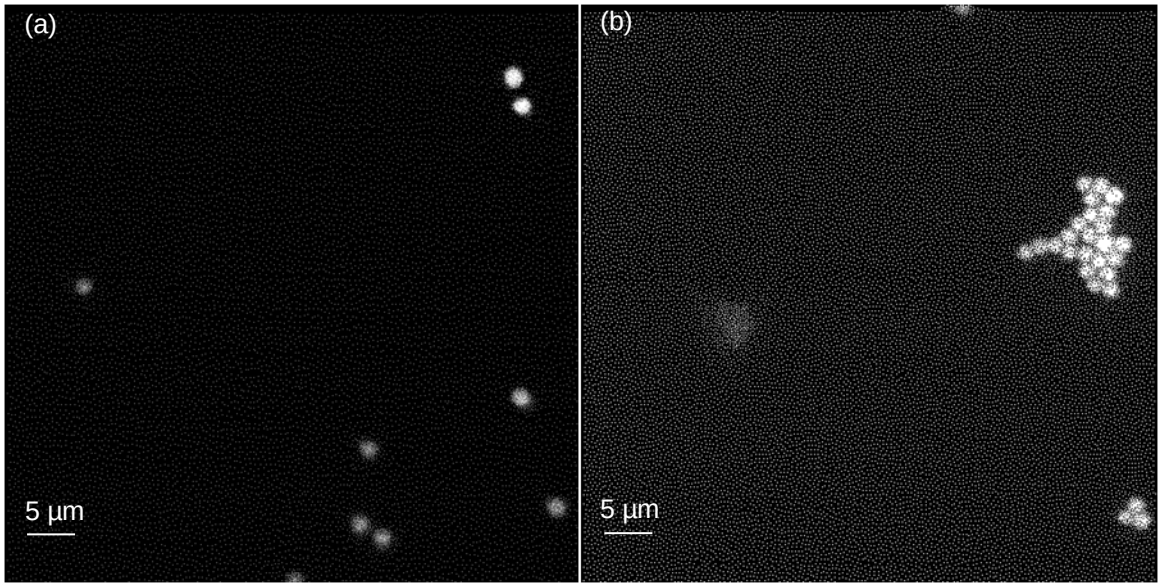



**Figure 38. Images of the same xy-position with different z positions. (a) is an imagine of green fluorescent beads placed on the bottom of a blank LiF disc at stage position +177 µm. (b) is an imagine of green fluorescent beads placed on top of a blank LiF disc at stage position -492 µm.**

## Results

Dosimetry foils and wires are responsive to high neutron fluences. The fluences experienced by the foils and wires only activated the Co dosimetry above the minimum detection limit. These fast flux measurements agreed with MCNP model predicted activation between 92% and 99%. A single data point is not preferred, but this agreement, initially, validates the MCNP model. Therefore, predictions of tracks based on the MCNP model are expected to be accurate.

Track counts using these values for notable particle sizes and exposures in the highest flux position in the sample ports are listed in Table 8.

Normal visible light images are not available with the CLSM, so reflected images were collected to assess particle size. An exemplary particle with tracks is presented in Figure 39. These 1.7 and 2.3 μm particles show 16 and 12 tracks respectively. Tracks are reliably conical; therefore, the fission

**Table 8. Model results for particles in the most intense flux position in the sample ports, as shown in the third position from the bottom of the sample port. Uranium enrichments selected comprise the majority of samples. Track counts use a 4π geometry.**

| Particle Diameter \ Exposure Time | Track Per Particle | | | | | |
|---|---|---|---|---|---|---|
| | 0.48% $^{235}U$ | 19.81% $^{235}U$ | 93.2% $^{235}U$ | Blank | Cr Inert | $^{232}Th$ |
| 1 μm / 1 Day | 0 | 0.1 | 0.6 | 0 | 0 | <0.01 |
| 10 μm / 1 Day | 3.2 | 118 | 555 | 0 | 0 | <0.01 |
| 1 μm / 3 Day | 0 | 0.1 | 1.7 | 0 | 0 | <0.01 |
| 10 μm / 3 Day | 9.4 | 354 | 1664 | 0 | 0 | <0.01 |

products' directions of travel can be identified. Particle size is estimated from the reflected image and shadow cast by the particle in the detector space. Due to diffraction, shadows are negligible for particles below 2 μm diameter in size enabling for full 2π geometry. Otherwise the shadow is corrected for by reducing the available geometry by the surface area of the particle produced in the xy-plane. A large shadow is observable in Figure 40. Figure 40a shows a cross-sectional view of a large 56 μm diameter particle. In the cross-section, tracks are readily visible around the edge, though in a 45° angled view, the shadow of the large particle is apparent in Figure 40b.

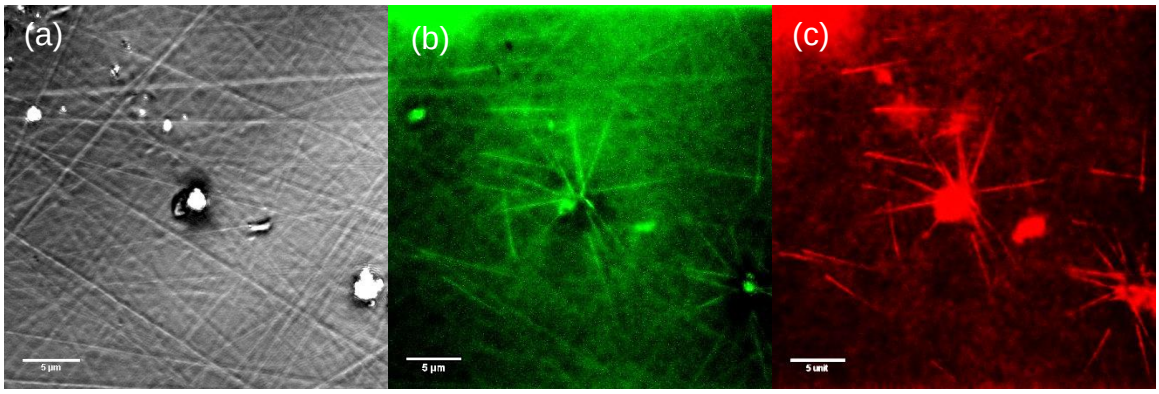



**Figure 39. Images of 93.2% $^{235}U$ particles of 1.7 and 2.3 µm diameters with fission tracks observed in the LiF detector, originating from the fuel particles. Fuel was irradiated with 4 x $10^8$ n $cm^{-2}$. Each image used individualized projection to best present particle and track signal. (a) is a reflected 488 nm light image projecting the max intensity voxel for a depth of 1.2 µm above and including the surface of the detector. (b) is $F_3^+$ signal summing the intensity for the first 9 µm of detector from the surface. (c) is $F_2$ signal projecting the max intensity voxel within the first 9 µm of detector from the surface. Scale bars are 5 µm.**

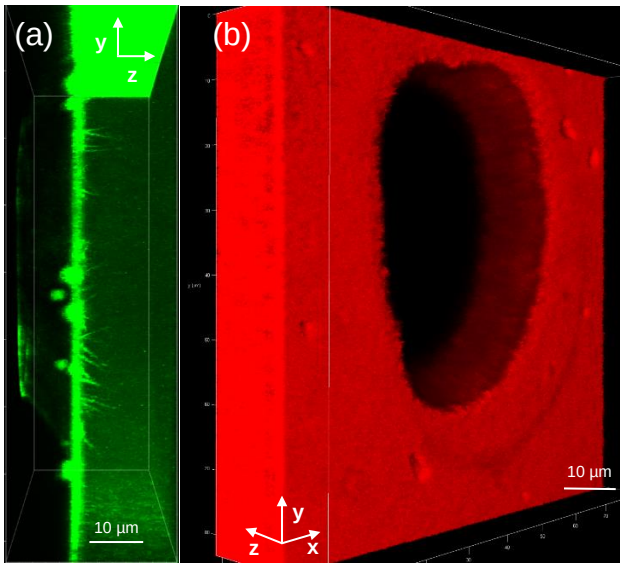



**Figure 40. 0.48% $^{235}U$ enriched particle projecting a shadow approximate to its surface area, 56 µm by 35 µm. (a) shows $F_3^+$ signal in cross-section with tracks along the end of the particle protruding into the LiF surface. (b) shows the $F_2$ signal at a 45° viewing angle to show that the shadow of the particle blocks signal over 20 µm into the detector.**

Many particles clearly did not have tracks associated with them like those in Figure 41. As the reflective characteristics of the particles matched those of other uranium particles across multiple light energies, those reflective particles were most likely uranium and were not sufficiently glued to the detector surface and, in turn, moved after irradiation. Additionally, the originating particles of the tracks present in Figure 41 are not present on the surface of the detector, which indicated that they moved again. In this image and in others, fission daughters may have traveled tens of microns in air before striking the detector at often an acute angle.

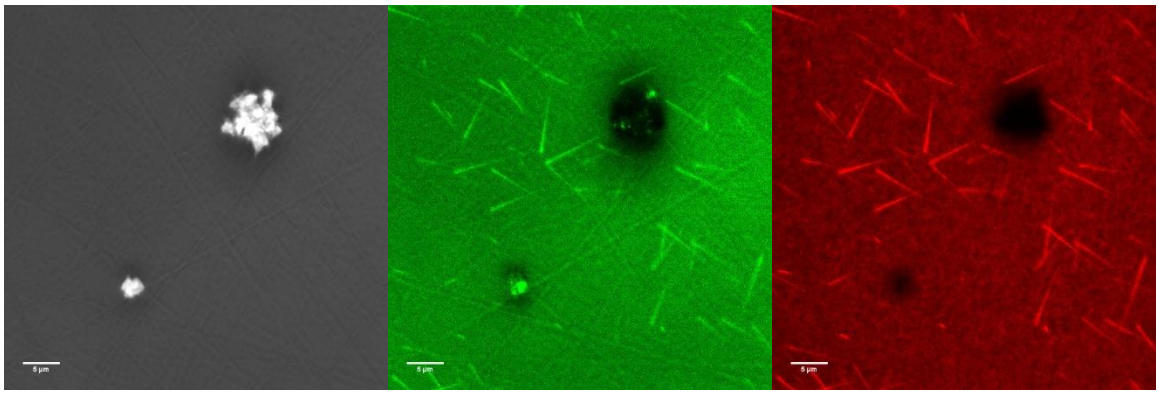


**Figure 41. images of 93.2% $^{235}U$ particles of 10 µm and 3 µm diameters with fission tracks observed in the LiF detector, tracks do not originate from the fuel particles. Fuel was irradiated with 4 x $10^8$ n $cm^{-2}$. Each image used a max intensity projection. (a) is a reflected 488 nm light image projecting the max intensity voxel for a depth of 11 µm above and including the surface of the detector. (b) is $F_3^+$ signal of the first 9 µm of detector from the surface. (c) is $F_2$ signal of the first 9 µm of detector from the surface. Scale bars are 5 µm.**

Ten particles with clearly associated tracks were identified, including the particles presented in Figure 39. They came from six different fluences using four different enrichments. One of the particles was observed by looking through the LiF disc and observing tracks on the top side of the sandwich of the disc. The number of particles is limited due to the high number of particles that were not associated with tracks and the long scan times. Particles and observed track information is listed in Table 9.

## Analysis

Particle adhesion to the surface of the disc presented the largest challenge to data collection and subsequent analysis. Under optical microscopy, cellulose nitrate was observed as an orange solid surrounding particles and making contact with the disc, but most particles did not have the cellulose present. For this reason, many particles moved after irradiation, which required long search times to find particles that had adhered to the discs. As shown in Figure 41, many particles could not be associated with tracks.

Viewing through the LiF detector reduced the resolution due to high light diffraction. Increasing laser intensity did have an appreciable effect on improving signal but did not improve resolution. As a result, while tracks could be observed in both sides of the detector, images of those sandwiches were poor in quality. Quantitative track analysis was not reliable when using this inspection method.

**Table 9. Reported observations and calculations for fission tracks from particles identified at various enrichments. Calculations use a $2\pi$ minus particle surface area detector geometry and particle size using an ellipsoid estimation.**

| % $^{235}$U | Particle Number | Particle Size [µm] | Estimated $^{235}$U Mass in Particle [fg] | Calculated Number of Fission Tracks | Observed Number of Fission Tracks |
|---|---|---|---|---|---|
| 0.48% | 3-1B-2-1 | 56 x 35 x 20 | 817.719 | 157 ± 12 | 96 |
| 0.48% | 3-1B-2-2 | 1 x 1 x 1 | 0.021 | 2 ± 15 in 100 particles | 1 |
| 0.48% | 3-1B3-1-1 | 1.7 x 1.4 x 1.4 | 0.07 | 7 ± 25 in 100 particles | 1 |
| 15.14% | 3-1C3-3-1 | 15 x 10 x 10 | 986.947 | 955 ± 31 | 162 |
| 19.81% | 3-1C-3-2 | 2.9 x 2.3 x 2 | 19.000 | 17 ± 4 | 21 |
| 93.28% | 3-1X-1 | 4.5 x 1.9 x 1.9 | 65.854 | 80 ± 9 | 15 |
| 93.28% | 3-1X-2 | 1.5 x 1.3 x 1.3 | 10.276 | 13 ± 4 | 19 |
| 93.28% | 3-1X-3 | 1.4 x 1.4 x 1.4 | 11.124 | 14 ± 4 | 7 |
| 93.28% | 3-1X3-1 | 1.7 x 1.6 x 1.6 | 17.642 | 22 ± 5 | 16 |
| 93.28% | 3-1X3-2 | 2.3 x 1.95 x 2 | 35.454 | 45 ± 7 | 12 |

Self-shielding from fuel particles presents the same difficulties seen in characterizing the Cf source from Chapter IV. Based on SRIM models, particles with a radius longer than 5.8 μm self-shield a percentage of tracks. To account for this, any particle with a radius greater than 5.8 μm had an elliptical volume from its center removed from the overall available fissionable mass. This volume increased with particle size. All particles are assumed to be homogenous solids; however, observations from Figure 36 show that this assumption may result in significant volume based error. A grain density of 8.3 g $cm^{-3}$ was used to estimate $^{235}U$ mass.

These limitations affect the accuracy and precision of enrichment calculations. Further analysis for enrichment relationships and predictions are discussed in Chapter VI.

# CHAPTER VI: ENRICHMENT RELATIONSHIPS

There are two primary ways to calculate enrichment by neutron bombardment. The first varies the ratio of thermal to fast neutrons. This creates a different number of fission tracks based on the amount of $^{235}U$ to $^{238}U$ present in the particle due to fission cross-section dependence on neutron energy. Crucially, this method does not require knowing the particles size or mass, and it overcomes complications like particle heterogeneity. However, this method requires multiple exposures and inspections. This experimental design was not logistically possible for the experiments described in Chapter V. The second method relates the number of tracks observed from a single exposure to the calculated mass based on the observed volume of each particle. In this analysis, particles are assumed to have a homogenous distribution of uranium isotopes throughout the observed particle. Additionally, particles mass is calculated from a volume that uses three observed particle diameters and assumes an ellipsoid approximation.

To calculate the number of tracks based on the particles size and known enrichment the following equation was used:

$$\boldsymbol{T_F = f_{235}(V_T - V_{ss})N_{235} \int \sigma_f dE\, \varphi_T \varepsilon_d} \qquad 8,$$

where $T_F$ is the predicted number of fission tracks; $f_{235}$ is the known enrichment percentage of $^{235}U$; $V_T$ is the total volume of the particle using an ellipsoid approximation $V_T = \frac{4}{3}\pi r_x r_y r_z$; $V_{ss}$ is the shielded interior of the particle also using an ellipsoid approximation $V_{ss} = \frac{4}{3}\pi(r_x - 8\,\mu m)\big(r_y - 8\,\mu m\big)(r_z - 8\,\mu m)$ where any axis greater than 5.8 μm forces a minimum approximation where any axis less than 5.8 μm is set to 5.9 μm; $N_{235}$ is the number of $^{235}U$ atoms per unit volume, $\sigma_f$ is 3 group integrated microscopic fission cross section for $^{235}U$ with respect to the neutron flux energy (this complex value is obtained by MCNP model); $\varphi_T$ is the

total neutron fluence experienced by the particle; and $\varepsilon_d$ is the 2π detector efficiency reduced by the particle shadow for particles with both x and y diameters larger than 2 μm. To calculate the number of atoms per unit volume, $N_{235} = \rho_{U_3O_8} N_A \%_{235} M_U$, the density $\rho_{U_3O_8}$ is multiple with Avagadro's number, percent $^{235}$U enrichment, and the molar mass U in $U_3O_8$.

Enrichment is factored out of Equation 8 is isolated to find the enrichment based on particle size, neutron fluence, and the number of tracks observed:

$$\%_{235} = \frac{T_F}{\varepsilon_d \varphi_T \int \sigma_f dE f_{235}(V_T - V_{ss}) \rho_{U_3O_8} N_A M_U} \quad 9$$

where $N_{235}$ is expanded and enrichment is separated so it can be solved. The enrichment values calculated using the values reported in Table 9 are presented in Table 10.

**Table 10. Reported observations and calculations for fission tracks from particles identified at various enrichments. Calculations use a 2π minus particle surface area detector geometry and particle size using an ellipsoid estimation.**

| $^{235}$U Particle Mass [fg] | Calculated Number of Fission Tracks | Known Enrichment | Observed Number of Fission Tracks | Predicted Enrichment based on tracks | Predicted Error |
|---|---|---|---|---|---|
| 817.719 | 107 ± 10 | 0.48% | 96 | 0.43% | 0.09% |
| 0.021 | 1 track from 2 ± 14 in 100 particles | 0.48% | 1 | 20.34% | 6.68% |
| 0.070 | 1 track from 6 ± 24 in 100 particles | 0.48% | 1 | 7.44% | 4.04% |
| 986.947 | 832 ± 29 | 15.14% | 194 | 2.57% | 1.05% |
| 19.000 | 24 ± 5 | 19.81% | 21 | 11.80 | 8.09% |
| 65.854 | 70 ± 8 | 93.28% | 15 | 17.39% | 22.24% |
| 10.276 | 11 ± 3 | 93.28% | 19 | 100.00% | 55.80% |
| 11.124 | 12 ± 3 | 93.28% | 7 | 47.22% | 53.63% |
| 17.642 | 19 ± 4 | 93.28% | 16 | 68.20% | 42.64% |
| 35.454 | 39 ± 6 | 93.28% | 12 | 50.55% | 29.77% |

A number of these values have notable errors which were difficult to characterize. Specifically, the large particles with relatively low track counts had better outcomes than the smaller particles due to the large number of tracks over large areas that did not approach saturation. Many larger particles of highly enriched uranium were saturated making track counting difficult.

The large depleted uranium particle agrees well with the observed track number. For the smaller particles, a large sampling size is vital since not all particles will have tracks. As a results the small sample sizes of small particles can over predict enrichment dramatically. This is a specific issue that cannot be resolved by fission track analysis unless a large number of tracks are created from a single particle. When observing a large number particles and small particles (diameters <1 μm) have a single track, Bayesian analysis may be used to assess the likelihood that one of these particles contains greater than a specified threshold of enrichment. To apply effectively, a large number of small particles, >100, should be inspected. To reasonably achieve a large area scan like this, a scan using the CLSM at the microscope's resonance threshold should be used.

Resonance scanning increases the voxel scan speed to 8000 hz. This solutions scalability is limited. While it can provide solutions to maintain resolution similar to that present in this work, with larger regions on the scale of thousands to tens of thousands of square microns in 5 to 20 minutes, it cannot reasonably scale to square centimeters. With current methods, resolution near the diffraction limit can be retained, but one square centimeter will take approximately two months to scan using the resonance mode. Although as eluded to in Chapter II, the de-excitation time required for our F-centers does not allow for faster scanning. Even with rigorous optimization of this method, it is reasonable to reduce this time to weeks.

Alternatively, the most preferred setup to optimize scan time would need a wide field, approximately 500 times water immersion objective using a silicon water surrogate immersion gel. Software would then need spherical aberration

correct used with a standard automatic focusing lens in front of a high-resolution, low-light avalanche diode type detector. In this way, square centimeters of xy-area may be collected with the first 5 to 10 microns of surface collected by viewing through the detector. Fortunately, a system similar to this exists for $Al_2O_3$:C,Mg. Landauer Inc.'s FNTD reader, Model FXR-700N, reads Al2)3:C,Mg detectors in rapid series with an automated loader capacity of 216 detectors. The system has a built in identification reader for each detector and will automatically recognize, scan, and process fluorescent images [59].

Currently, this method of enrichment investigation requires more analysis to predict enrichments accurately. Samples are available for further analysis as the scan time to investigate all samples created using current methods is in excess of ten years. Preferably, lessons learned from uranium experiments should be used to produce ten highly controlled samples where each grain of uranium is individually controlled and discs are prepared in a highly controlled manner consistent with IAEA methods discussed in this work.

Regardless of the current level of accuracy when predicting enrichment from fission tracks only, the methodology developed through this work is highly desirable in traditional lab-based safeguards fission track analysis. Many labor intensive steps required when using etchable track detectors are removed, notably the registration requirements, making FNTD highly desirable for current lab based fission track analysis.

## Future Work

Continuation of this work should focus on the following areas. Tasks are described within the context of graduate research efforts. Tasks are not sequential or listed by priority.

- Develop a first-principles model using electron band behavior for fluorescing defects, focusing on Ferknel defects, coupled with a heavy ion radiolytic damage model that predicts the fluorescing period, excitation

profile, stoke shift, emission profile of LiF, with the target of developing a model for any recurring lattice structure.

- Develop an image analysis program to pick out and analyze fission track and alpha tracks using thermally treated samples.
- Design a semi-autonomous system to induct an environmental air filter or soil sample, irradiate for a prescribed particle of fuel, inspect the detector, analyze the results, and predict enrichment of any particle that meets the user's criteria.
- Build the system described above.

A straight forward design of the system based on this method to replace current etchable track detector procedures would employ two steps involving a technician. This tool would require a technician to extract from an environmental sample. Extraction may be wet or dry. These methods may include one or a combination of filtration, sonication, wet ashing, thermal separation, inertial separation, or other methods. The remaining sample would be dried if needed and distributed onto a plastic sheet. This sheet would be placed on one LiF detector ($2\pi$ configuration) and irradiated with approximately $10^{14}$ neutrons with roughly a 15 to 85 thermal to fast flux spectrum. The sample would be removed and placed onto, preferable a coaxial CLSM-LAMS stage. From below the LiF detector, the CLSM would scan just below the detector surface containing fuel. This would be a very low and fast resolution scan. The CLSM would identify volumes where $F_2$ and $F_3^+$ are concentrated, roughly three times background and would utilize LAMS to analyze the particle immediately. With previous matrix characterization for the LiF and glue, the LAMS can quickly analyze the sample for fissile material content. This tool would enable rapid sample throughput and reduce the bottleneck seen at safeguard labs around the world.

# REFERENCES

[1] E. G. Yukihara and S. W. S. McKeever, *Optically stimulated luminescence : fundamentals and applications*. Wiley, 2011.
[2] S. A. Durrani and R. K. Bull, *Solid state nuclear track detection : principles, methods, and applications*. Pergamon Press, 1987.
[3] R. F. Galbraith, *Statistics for Fission Track Analysis - Rex F. Galbraith - Google Books*. University College London, UK: Chapman & Hall/CRC, 2005.
[4] R. L. (Robert L. Fleischer, P. B. Price, and R. M. Walker, *Nuclear tracks in solids : principles and applications*. University of California Press, 1975.
[5] M. F. L'Annunziata, *Handbook of radioactivity analysis*. .
[6] K. Gallagher, R. Brown, and C. Johnson, "FISSION TRACK ANALYSIS AND ITS APPLICATIONS TO GEOLOGICAL PROBLEMS," *Annu. Rev. Earth Planet. Sci.*, vol. 26, no. 1, pp. 519–572, May 1998.
[7] I. Dokic, M. Niklas, F. Zimmermann, A. Mairani, P. Seidel, D. Krunic, O. Jäkel, J. Debus, S. Greilich, and A. Abdollahi, "Correlation of Particle Traversals with Clonogenic Survival Using Cell-Fluorescent Ion Track Hybrid Detector.," *Front. Oncol.*, vol. 5, p. 275, 2015.
[8] D. A. Young, "Etching of radiaton damage in lithium fluoride," *Nature*, vol. 182, no. 4632, pp. 375–377, 1958.
[9] N. Dzigal, E. Chinea-Cano, S. Walsh, and A. Limbeck, "Revisiting the fission track method for the analysis of particles in safeguards environmental samples," *Talanta*, vol. 167, no. November 2016, pp. 583–592, May 2017.
[10] O. Stetzer, M. Betti, J. Van Geel, N. Erdmann, J. V. Kratz, R. Schenkel, and N. Trautmann, "Determination of the 235U content in uranium oxide particles by fission track analysis," *Nucl. Instruments Methods Phys. Res. Sect. A Accel. Spectrometers, Detect. Assoc. Equip.*, vol. 525, no. 3, pp. 582–592, 2004.
[11] F. Esaka, D. Suzuki, T. Yomogida, and M. Magara, "Application of automated particle screening for effective analysis of individual uranium particles by thermal ionization mass spectrometry," *Anal. Methods*, vol. 8, pp. 1543–1548, 2016.
[12] C.-G. Lee, D. Suzuki, F. Esaka, M. Magara, N. Shinohara, and S. Usuda, "Selective Detection of Particles Containing Highly Enriched Uranium for Nuclear Safeguards Environmental Samples," *J. Nucl. Sci. Technol.*, vol. 46, no. 8, pp. 809–813, 2009.
[13] S.-L. Guo, S.-H. Zhou, W. Meng, S.-F. Sun, and R.-F. Shi, "Detection efficiencies of solid state nuclear track detectors for fission fragments," *Nucl. Tracks*, vol. 5, no. 4, p. 358, Dec. 1981.
[14] D. Nikezic and K. N. Yu, "Formation and growth of tracks in nuclear track materials," *Mater. Sci. Eng. R Reports*, vol. 46, no. 3, pp. 51–123, 2004.
[15] INTERNATIONAL ATOMIC ENERGY AGENCY, "Safeguards Techniques And Equipment: 2011 Edition," VIENNA, 2011.
[16] L. Tommasino and C. Armellini, "A new etching technique for damage track

detectors," *Radiat. Eff.*, vol. 20, no. 4, pp. 253–255, Jan. 1973.
[17] C. Lee, D. Suzuki, F. Esaka, M. Magara, and S. Usuda, "Selective Detection of Particles Containing Highly Enriched Uranium for Nuclear Safeguards Environmental Samples Selective Detection of Particles Containing Highly Enriched Uranium," vol. 3131, no. April 2016, 2012.
[18] H. A. Khan and S. A. Durrani, "Efficiency calibration of solid state nuclear track detectors," *Nucl. Instruments Methods*, vol. 98, no. 2, pp. 229–236, Jan. 1972.
[19] International Atomic Energy Agency, "Occupational Radiation Exposure Monitoring Website." [Online]. Available: http://www-ns.iaea.org/tech-areas/rw-ppss/occ-rad-exposure-monitoring.asp?s=3. [Accessed: 08-Jun-2017].
[20] J. A. Nieto, "Thermoluminescence Dosimetry (TLD) and its Application in Medical Physics," in *AIP Conference Proceedings*, 2004, vol. 724, pp. 20–27.
[21] V. Pagonis, R. Chen, and J. L. Lawless, "Superlinear dose response of thermoluminescence (TL) and optically stimulated luminescence (OSL) signals in luminescence materials: An analytical approach," *J. Lumin.*, vol. 132, pp. 1446–1455, 2012.
[22] L. A. DeWerd and T. G. Stoebe, "Thermoluminescent Properties of Solids and Their Applications: Thermoluminescence, used in such applications as the measurement of ionizing radiation, the dating of ancient artifacts, and in geological studies, depends upon the defect properties of solids on JSTOR," *Am. Sci.*, vol. 60, no. 3, pp. 303–310, 1972.
[23] L. Bøtter-Jensen, S. W. S. McKeever, and A. G. Wintle, *Optically stimulated luminescence dosimetry*. Elsevier, 2003.
[24] S. V Boichenko, K. Koenig, S. A. Zilov, V. P. Dresvianskiy, A. P. Voitovich, A. L. Rakevich, A. V Kuznetsov, A. V Bartul, and E. F. Martynovich, "Study of the fluorescence blinking behavior of single $F_2$ color centers in LiF crystal," *J. Phys. Conf. Ser.*, vol. 552, p. 12048, 2014.
[25] F. Preusser, "Bleaching characteristics of some optically stimulated luminescence signals," *Anc. TL*, vol. 17, no. 1, pp. 11–14, 1999.
[26] A. A. Omotayo, J. E. Cygler, and G. O. Sawakuchi, "The effect of different bleaching wavelengths on the sensitivity of Al2O3:C optically stimulated luminescence detectors (OSLDs) exposed to 6 MV photon beams," *Med. Phys.*, vol. 39, no. 9, pp. 5457–5468, Aug. 2012.
[27] A. J. J. Bos, M. Proki, and J. C. Brouwer, "OPTICALLY AND THERMALLY STIMULATED LUMINESCENCE CHARACTERISTICS OF MgO : Tb 3þ."
[28] G. M. Akselrod, M. S. Akselrod, E. R. Benton, and N. Yasuda, "A novel Al2O3 fluorescent nuclear track detector for heavy charged particles and neutrons," *Nucl. Instruments Methods Phys. Res. Sect. B Beam Interact. with Mater. Atoms*, vol. 247, no. 2, pp. 295–306, Jun. 2006.
[29] L. C. Oliveira and O. Baffa, "A new luminescent material based on CaB6O10:Pb to detect radiation," *J. Lumin.*, vol. 181, pp. 171–178, 2017.

[30] M. S. Akselrod and G. J. Sykora, “Fluorescent nuclear track detector technology – A new way to do passive solid state dosimetry,” *Radiat. Meas.*, vol. 46, no. 12, pp. 1671–1679, Dec. 2011.
[31] P. Bilski and B. Marczewska, “Fluorescent detection of single tracks of alpha particles using lithium fluoride crystals,” *Nucl. Instruments Methods Phys. Res. Sect. B Beam Interact. with Mater. Atoms*, vol. 392, pp. 41–45, Feb. 2017.
[32] J. A. Bartz, C. J. Zeissler, V. V Fomenko, and M. S. Akselrod, “An imaging spectrometer based on high resolution microscopy of fl uorescent aluminum oxide crystal detectors,” *Radiat. Meas.*, vol. 56, pp. 273–276, 2013.
[33] J. M. Osinga, M. S. Akselrod, R. Herrmann, V. Hable, G. Dollinger, O. Jäkel, and S. Greilich, “High-accuracy fluence determination in ion beams using fluorescent nuclear track detectors,” *Radiat. Meas.*, vol. 56, pp. 294–298, 2013.
[34] K. Schwartz, J. Maniks, and I. Manika, “A review of colour center and nanostructure creation in LiF under heavy ion irradiation,” *Phys. Scr.*, vol. 90, no. 9, p. 94011, 2015.
[35] R. L. Fleischer, P. B. Price, and R. M. Walker, *Nuclear Tracks in Solids: Principles and Applications*. .
[36] G. Baldacchini, E. De Nicola, R. M. Montereali, A. Scacco, and V. Kalinov, “Optical bands of F2 and F3+ centers in LiF,” *J. Phys. Chem. Solids*, vol. 61, pp. 21–26, 2000.
[37] K. Schwartz, C. Trautmann, R. Neumann, M. Toulemonde, and W. Knolle, “Color-center creation in LiF under irradiation with swift heavy ions : Dependence on energy loss and fluence,” vol. 184104, pp. 1–8, 2004.
[38] R. M. Montereali, F. Bonfigli, F. Menchini, and M. A. Vincenti, “Optical spectroscopy and microscopy of radiation-induced light-emitting point defects in,” vol. 779, no. 2012, 2015.
[39] N. Itoh and A. M. Stoneham, *Materials Modification by Electronic Excitation - Noriaki Itoh, Marshall Stoneham - Google Books*. Cambridge: Cambridge University Press, 2001.
[40] Precision Micro-Optics, “Lithium Fluoride.” [Online]. Available: http://www.pmoptics.com/Lithium_Fluoride.html. [Accessed: 08-Jun-2017].
[41] A. B. Kunz, T. Miyakawa, and S. Oyama, “Electronic Energy Bands, Excitons, and Plasmons in Lithium Fluoride Crystal,” *Phys. status solidi*, vol. 34, no. 2, pp. 581–589, 1969.
[42] A. Neuholz and S. Greilich, “Assessment of microscopic ion beam field variation using fluorescent nuclear track detectors,” 2017.
[43] Microscopy U, “Introductory Confocal Concepts | MicroscopyU.” [Online]. Available: https://www.microscopyu.com/techniques/confocal/introductory-confocal-concepts. [Accessed: 08-Jun-2017].
[44] Leica Microsystems CMS GmbH, “Leica TCS SP8 Scan Head Poster.” Leica Microsystems CMS GmbH, Mannheim, 2015.

[45] R. T. Borlinghaus, H. Birk, and F. Schreiber, “Detectors for Sensitive Detection : HyD,” 2012.
[46] MicroscopyU, “The Diffraction Barrier in Optical Microscopy | MicroscopyU.” [Online]. Available: https://www.microscopyu.com/techniques/super-resolution/the-diffraction-barrier-in-optical-microscopy. [Accessed: 08-Jun-2017].
[47] G. Baldacchini, S. Bigotta, and R. M. Montereali, “Emission decay times of F 2 color centers in heavily irradiated LiF crystals,” vol. 95, pp. 299–303, 2001.
[48] X-5 Monte Carlo Team, “MCNP — A General Monte Carlo N-Particle Transport Code, Version 5 Volume I: Overview and Theory,” 2008.
[49] J. F. Ziegler, M. D. Ziegler, and J. P. Biersack, “SRIM - The stopping and range of ions in matter (2010),” *Nucl. Instruments Methods Phys. Res. Sect. B Beam Interact. with Mater. Atoms*, vol. 268, no. 11–12, pp. 1818–1823, 2010.
[50] E. Browne, V. S. Shirley, and C. M. Lederer, *Table of isotopes*, 7th ed. New York: Wiley, 1978.
[51] J. Schindelin, I. Arganda-Carreras, E. Frise, V. Kaynig, M. Longair, T. Pietzsch, S. Preibisch, C. Rueden, S. Saalfeld, B. Schmid, J.-Y. Tinevez, D. J. White, V. Hartenstein, K. Eliceiri, P. Tomancak, and A. Cardona, “Fiji: an open-source platform for biological-image analysis.,” *Nat. Methods*, vol. 9, no. 7, pp. 676–82, Jun. 2012.
[52] J. A. Bartz, S. Kodaira, M. Kurano, N. Yasuda, and M. S. Akselrod, “High resolution charge spectroscopy of heavy ions with FNTD technology,” *Nucl. Instruments Methods Phys. Res. Sect. B Beam Interact. with Mater. Atoms*, vol. 335, pp. 24–30, Sep. 2014.
[53] C. Trautmann, K. Schwartz, J. M. Costantini, T. Steckenreiter, and M. Toulemonde, “Radiation defects in lithium fluoride induced by heavy ions,” *Nucl. Instruments Methods Phys. Res. Sect. B Beam Interact. with Mater. Atoms*, vol. 146, no. 1–4, pp. 367–378, 1998.
[54] K. Schwartz, C. Trautmann, T. Steckenreiter, and M. Kra, “Damage and track morphology in LiF crystals irradiated with GeV ions,” vol. 58, no. 17, pp. 232–240, 1998.
[55] J. D. Burns, S. M. Van Cleve, E. H. Smith, and R. A. Boll, “Californium purification and electrodeposition,” *J. Radioanal. Nucl. Chem.*, pp. 109–116, 2015.
[56] J. F. Ziegler, M. D. Ziegler, and J. P. Biersack, “SRIM - The stopping and range of ions in matter (2010),” *Nucl. Instruments Methods Phys. Res. Sect. B Beam Interact. with Mater. Atoms*, vol. 268, no. 11–12, pp. 1818–1823, 2010.
[57] K. Schwartz, M. Lang, R. Neumann, M. V. Sorokin, C. Trautmann, A. E. Volkov, and K. O. Voss, “Damage creation in LiF and NaCl crystals irradiated with swift heavy ions at 8 and 300 K,” *Phys. Status Solidi Curr. Top. Solid State Phys.*, vol. 4, no. 3, pp. 1105–1109, 2007.

[58] M. Lipponen and S. Lehto, “Development of a track-etch method for extracting uranium containing particles from swipes. Development of a SIMS method for isotopic analysis of uranium containing particles,” Helsinki, Finland, 2002.
[59] M. S. Akselrod, “FNTD Technology - Latest Advances in Instrumentation and Neutron-Photon Discrimination,” in *26th International Conference on Nuclear Tracks in Solids*, 2014, pp. 30–31.

# VITA

Jonathan Gill graduated from the United States Military Academy in 2005 with a Bachelor of Science in Nuclear Engineering. Following graduation, Jonathan served for 8 years as an Army Engineer Officer. During this time he earned a Master's of Science in Engineering Management from the Missouri University of Science and Technology. In 2014, he enrolled at the University of Tennessee to pursue his Doctorate and a concurrent Master's of Science in Nuclear Engineering. Jonathan master's degree compared methods for dissolution for post-detonation nuclear weapons debris. He pursued his doctorate with BWX Technologies Inc. on development of fluorescing fission track detectors. His interests in the nuclear field focus on nuclear security applications for special nuclear materials and post-detonation analysis.